Tectonics

RESEARCH ARTICLE
10.1029/2022TC007498

Paleozoic Geodynamics and Architecture of the Southern Part of the Mongolian Altai Zone

T. Sukhbaatar[1,2], O. Lexa[1], K. Schulmann[2], C. Aguilar[2,3], P. Štípská[2], J. Wong[4], Y. Jiang[5], J. Míková[2], and D. Zhao[4]

[1]Institute of Petrology and Structural Geology, Charles University, Prague, Czech Republic, [2]Czech Geological Survey, Prague, Czech Republic, [3]Department of Mineralogy, Petrology and Applied Geology, Faculty of Earth Sciences, University of Barcelona, Barcelona, Spain, [4]Department of Earth Sciences, The University of Hong Kong, Hong Kong, China, [5]State Key Laboratory of Isotope Geochemistry, Guangzhou Institute of Geochemistry, Chinese Academy of Sciences, Guangzhou, China

Abstract The Mongolian Altai Zone of the Central Asian Orogenic Belt has been traditionally interpreted as a mosaic of Paleozoic magmatic arcs, back-arcs, and Precambrian continental terranes. In order to define its architecture and its tectonic evolution, three domains previously interpreted as terranes were investigated. The findings show that the Northern and Central domains are formed by a metamorphic sequence characterized by Barrovian S1 fabric transposed by recumbent folds and dominant sub-horizontal amphibolite facies S2 schistosity. The latter is associated with the intrusions of late Devonian syntectonic granite sheets and anatexis in the south. The Southern domain is formed by early Permian migmatites and anatectic granites separated from the metamorphic envelope by amphibolite to green-schist facies D3 shear zone cross-cutting S2 fabrics. All domains have been reworked by E-W upright folds associated with axial-planar greenschist facies cleavage, reflecting the final mid-Permian to Triassic D4 shortening. Lithological, geochemical, and U-Pb zircon analyses of metasediments of all domains indicate that they are formed by Ordovician mature quartzite derived from Precambrian basement intruded by Cambrian-Ordovician continental arc and Silurian immature graywacke which originated through erosion of an oceanic arc. Altogether, the whole sequence represents a fore-arc basin in front of a migrating arc affected by thickening and late Devonian extension. The Southern domain is interpreted as an early Permian core complex amplified by mid-Permian to Triassic compression. The apparent "terrane" architecture of the Mongol Altai Zone originated due to Devonian and Permian heterogeneous reworking of a giant Ordovician to Silurian fore-arc basin.

Key Points:

- The Mongolian Altai Zone is an Ordovician to Silurian fore-arc basin affected by Barrovian prograde metamorphism
- Late Devonian extension resulted in intrusion of sub-horizontal, syntectonic granite sheets and partial melting in deep crustal levels
- Early Permian extension resulted in the formation of metamorphic core complex later amplified by regional mid-Permian to Triassic compression

Supporting Information:

Supporting Information may be found in the online version of this article.

Correspondence to:

T. Sukhbaatar,
sukhbaat@natur.cuni.cz

Citation:

Sukhbaatar, T., Lexa, O., Schulmann, K., Aguilar, C., Štípská, P., Wong, J., et al. (2022). Paleozoic geodynamics and architecture of the southern part of the Mongolian Altai Zone. *Tectonics*, *41*, e2022TC007498. https://doi.org/10.1029/2022TC007498

Received 11 JUL 2022
Accepted 21 JUL 2022

Author Contributions:

Conceptualization: T. Sukhbaatar, O. Lexa, K. Schulmann
Data curation: T. Sukhbaatar, O. Lexa
Formal analysis: T. Sukhbaatar, J. Wong, J. Míková, D. Zhao
Funding acquisition: O. Lexa, K. Schulmann
Investigation: T. Sukhbaatar, O. Lexa, K. Schulmann
Methodology: T. Sukhbaatar, C. Aguilar, J. Wong, J. Míková, D. Zhao
Project Administration: O. Lexa, K. Schulmann

1. Introduction

An important component of all accretionary systems is the up to 20 km-thick volcanic-sedimentary wedge built above the subducting plate, in front of a magmatic arc and upper plate continent (Cawood et al., 2009). This wedge, often several thousand kilometers long and hundreds of kilometers wide, is accreted during the *ca*. 100 Ma lifetime of oceanic spreading and subduction (Kusky et al., 2013). The main wedge feature is the so-called ocean plate stratigraphy with the oldest pillow lavas, bedded cherts, deep marine siliceous fine-grained sediments, and the youngest turbidites derived from a continent and magmatic arc. This sequence is often imbricated together with seamount volcanic products, and is later intruded by an oceanward migrating magmatic arc due to a continuous rollback of a subducting plate. The entire process produces a typical lithological association of Pacific-type active margins (Collins, 2002).

Based on this, a classical Japan Islands-type scenario was proposed for the volcano-sedimentary accretionary prism of the Mongolian Altai Zone, one of the main constituents of the Mongolian Collage System (Long et al., 2007; Xiao, Kusky, et al., 2015). The Mongolian Altai Zone consists mainly of thick late Cambrian and Ordovician sedimentary packages covered by Silurian and Devonian volcano-clastic sequences (Badarch et al., 2002; Byamba, 2009; Jiang et al., 2017; Tomurtogoo, 2012). It has been proposed that this volcanic-sedimentary wedge formed due to the continuous subduction of an oceanic plate beneath a string of Mongolian continents and a late Proterozoic to early Cambrian oceanic unit called the Lake Zone (Khukhuudei et al., 2020; Kovalenko et al., 1996; Ruzhentsev & Burashnikov, 1996; Zonenshain et al., 1990) which was intruded by the 1,800 km-long magmatic arc (Janoušek et al., 2018; Rudnev, Babin, et al., 2013; Rudnev et al., 2009; Rudnev, Kovach, & Ponomarchuk, 2013). Erosion of the arc and basement continental crust then produced detrital material that was

Resources: T. Sukhbaatar, O. Lexa, K. Schulmann
Software: T. Sukhbaatar, O. Lexa
Supervision: O. Lexa, K. Schulmann
Validation: T. Sukhbaatar, O. Lexa, K. Schulmann
Visualization: T. Sukhbaatar, O. Lexa
Writing – original draft: T. Sukhbaatar, O. Lexa, K. Schulmann, C. Aguilar
Writing – review & editing: T. Sukhbaatar, O. Lexa, K. Schulmann, C. Aguilar, P. Štípská, Y. Jiang

filling the wedge throughout the entire early Paleozoic (Jiang et al., 2017; Kozakov et al., 2009; Long et al., 2020; Soejono et al., 2018). However, the sedimentary constituents of the wedge were not directly examined in terms of the presence of main components of ocean plate stratigraphy. Instead, the differences in stratigraphic evolutions were interpreted indirectly in terms of the juxtaposition of various tectono-stratigraphic terranes (Badarch et al., 2002). In addition, the Mongolian Altai Zone, along with the closely situated Chinese Altai Zone, both experienced Silurian to Devonian magmatism that was interpreted as a result of oceanic rollback associated with the migration of magmatic arc across the wedge (Cai et al., 2015). This thermal event was also responsible for metamorphism and partial melting of fertile sedimentary rocks, leading to the formation of large metamorphic units and intrusions of granitoids in all crustal levels (Burenjargal et al., 2014; Hanžl et al., 2016; Jiang et al., 2015, 2010; Kozakov et al., 2002, 2009, 2019; M. Sun et al., 2008). The southern part of the Chinese Altai Zone was finally reworked during the Permian-Triassic event (Broussolle et al., 2019 and references therein; Kozakov et al., 2011), but its extent and contribution to the transformation of the accretionary system into a mature crust in the Mongolian Altai Zone remain unknown.

In this study, we investigated the narrow, 42 km-long NNW-SSE section of the Mongolian Altai Zone in southwestern Mongolia to characterize the lithological variations and geochronological records of igneous and metasedimentary rocks of three domains previously interpreted as distinct tectono-stratigraphic terranes. The findings are supported by detailed structural analysis, which allows better characterization of the geological archive of individual crustal levels. In particular, the high mountain peaks reaching around 3,000 m in the central part of the section allow us to examine different vertical levels from the structurally deepest parts in the southern Gobi plain to the uppermost crustal levels at the crest of the mountains. This topographical situation represents a unique opportunity to examine the structure and lithological content of the wedge in three dimensions and to understand its architecture and tectonic evolution.

2. Geological Setting

The Central Asian Orogenic Belt (e.g., Jahn et al., 2004; Khain et al., 2003; Mossakovsky et al., 1993; Windley et al., 2007), or the Altaids (Sengor & Natalin, 1996; Sengör et al., 1993), extends from the Siberian craton in the north to the Tarim and North China cratons in the south, and from the Okhotsk Sea in the east to the Ural mountains in the west. Its formation began in the late Neoproterozoic and terminated in the Triassic in response to the collision of the Siberian and North China continents (Wilhem et al., 2012). It was formed by the amalgamation of island arcs, ophiolitic belts, accretionary complexes, back-arc and fore-arc basins, and Precambrian micro-continents along a long-lived convergent margin during several successive accretionary phases (Figure 1; Badarch et al., 2002; Windley et al., 2007; Xiao et al., 2018). These accretionary phases are characterized by discontinuous high-P belts ranging in age from early Paleozoic in the north (e.g., Khain et al., 2003) to late Paleozoic in the south (e.g., J. Gao & Klemd, 2003), and by a wide zone of Devonian-Carboniferous metamorphic rocks in the central part of the orogen.

The northern part of the Mongolian Collage System is composed of Precambrian continental blocks (called the Central Mongolian Massif [CMM]; Tomurtogoo, 2014, 2017) which are fringed in the south and west by Neoproterozoic ophiolitic belts and arc complexes known as the Lake Zone (Buriánek et al., 2017; Dijkstra et al., 2006; Khain et al., 2003; Khukhuudei et al., 2022; Kovach et al., 2011; Tomurtogoo, 2012; Yarmolyuk et al., 2011; Zonenshain & Kuzmin, 1978). Both the Precambrian basement blocks and the Lake Zone are intruded by *ca*. 530 to 460 Ma granitic plutons (Rudnev, Babin, et al., 2013; Rudnev et al., 2012; Soejono et al., 2017), called the later Ikh Mongol arc (Janoušek et al., 2018), which are connected to regional high temperature-low pressure H*T*-L*P* metamorphism (Kozakov et al., 2012). Further to the south, the Chinese and Mongolian Altai zones occur, bounded by the Bulgan/Erquis fault zones from the Trans-Altai Zone and East Junggar domain, both consisting of Devonian and Carboniferous volcanic-sedimentary sequences imbricated with Cambrian to Devonian ophiolites (Guy et al., 2021; Lehmann et al., 2010). Finally, the southernmost part of the Mongolian Collage System is formed by the South Gobi Zone with Grenvillean-age continental crust and its early Paleozoic volcanic-sedimentary cover (Rojas-Agramonte et al., 2011).

The early accretionary evolution of the Mongolian Collage System is characterized by early Cambrian thrusting of the Lake Zone over the Precambrian continental blocks (e.g., Dijkstra et al., 2006; Khomentovsky & Gibsher, 1996; Khukhuudei et al., 2020, 2022; Štípská et al., 2010; Tomurtogoo, 1980). This was followed by a

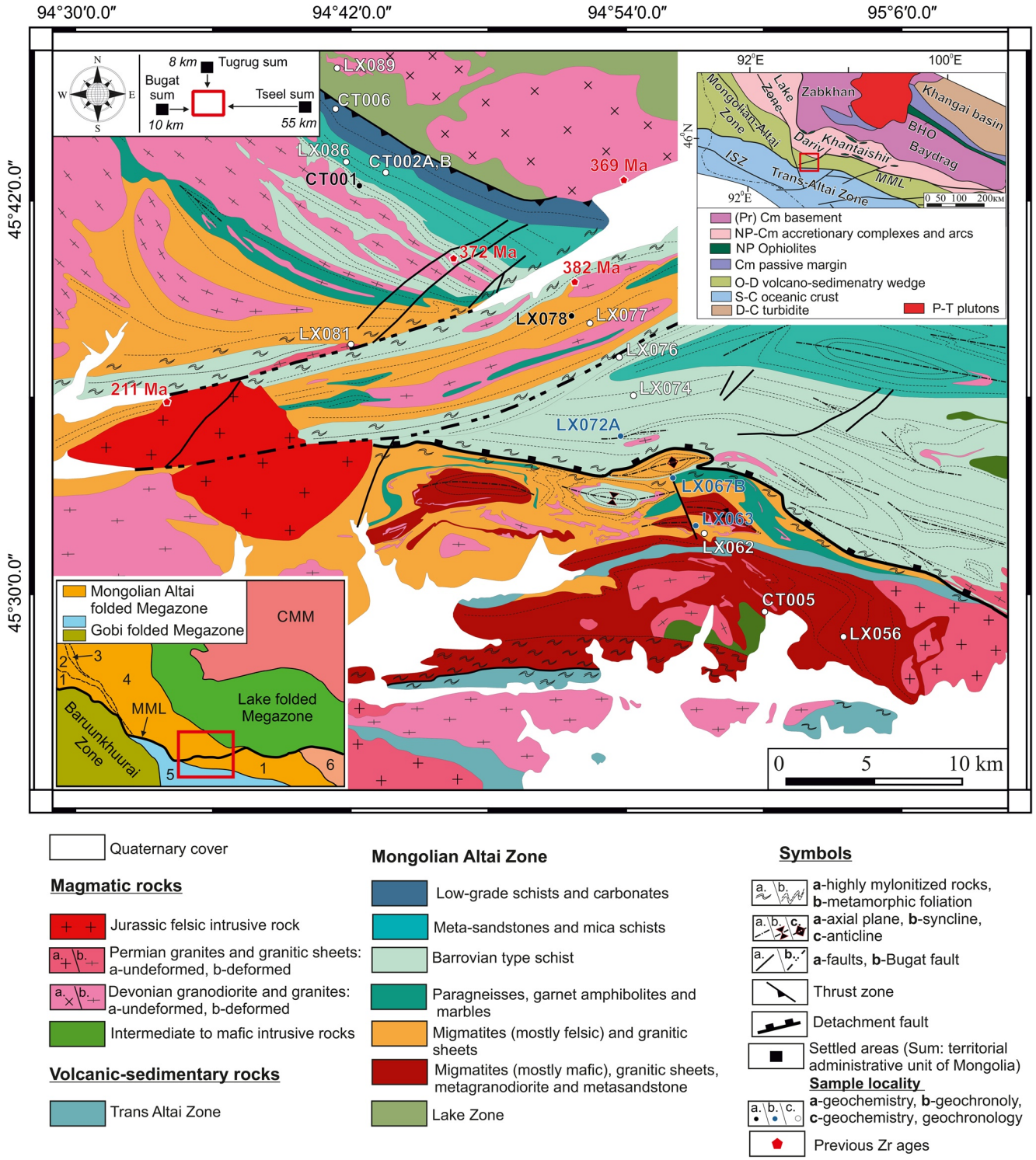

Figure 1. Simplified geological map of the studied area showing the main lithostratigraphic units (modified after Togtokh et al., 1993). The location of samples for geochemistry and/or geochronology (compiled in Table 1) and previous zircon ages (compiled in Table 2) are shown. The upper right inset shows the location of the studied area in the Mongolian Altai Zone of the Central Asian Orogenic Belt (BHO, Bayankhongor ophiolite zone, ISZ, Irtysh shear zone, and MML, Main Mongolian Lineament) delineated by a red square (modified after Buriánek et al., 2017; Kröner et al., 2010). The lower left inset shows the simplified tectonic scheme of the western part of Mongolia (modified after Tomurtogoo, 2017; red rectangle - studied area; CMM, Central Mongolian Massif, 1 - Bodonch-Tseel Zone, 2 - Tavanbogd Zone, 3 - Ulgii Zone, 4 - Hovd Zone, 5 - Edren Zone, and 6 - Gichgene-Matad Zone).

long-lasting Cambrian-Ordovician oceanic subduction, resulting in the formation of the Cambrian-Ordovician Ikh Mongol arc system, which intruded the SW margin (in current coordinates) of the CMM together with Lake Zone ophiolite complexes (Janoušek et al., 2018). Simultaneously, fore-arc volcanic-sedimentary sequences were deposited in both the Mongolian and Chinese Altai zones (Jiang et al., 2017; Soejono et al., 2018). This sedimentary evolution was terminated by the deposition of Silurian-Devonian back-arc and passive margin sequences (Buriánek et al., 2022). Subsequently, the Devonian–early Carboniferous arcs and back-arcs formed in the Trans-Altai Zone in Mongolia and the East Junggar domain in NW China (Nguyen et al., 2018; Xiao et al., 2009). The late Paleozoic final amalgamation is associated with major shortening and deformation of the entire system (Guy et al., 2020; Xiao, Kusky, et al., 2015).

2.1. Geology of the Mongolian Altai Zone in Southwestern Mongolia

The differences in lithostratigraphy and metamorphic evolution along the strike of the Mongolian Altai Zone led Badarch et al. (2002) to divide it into three distinct units called the Hovd, Gobi-Altai, and Tseel tectono-stratigraphic terranes. Alternatively, the Mongolian Altai Zone has also been tectonically divided by Tomurtogoo (2017) into five terranes which are, from north to south: the Tsagaanshuvuut, Hovd, Ulgii, Tavanbogd, and Bodonch-Tseel zones (Figure 1, lower left inset). While the Hovd and Tavanbogd zones are dominated mainly by Cambrian and Ordovician siliciclastic sequences, the Ulgii zone is characterized by Devonian terrigenic-carbonate sediments similar to those of the Gichigene formation of the Gobi-Altai terrane (Buriánek et al., 2022). In this study, the target domain comprises a junction of four main litho-stratigraphy zones: the Ulgii and Hovd zones in the west, the Gobi-Altai terrane in the east (Badarch et al., 2002), and the high-grade Bodonch-Tseel zone in the south (Tomurtogoo, 2017). To avoid confusion between the terminology of Badarch et al. (2002) and Tomurtogoo (2017), we prefer to use the term "domain" in this article, instead of the overused terms "terrane" or "zone." The Hovd domain stratigraphy is defined by Cambrian basic and felsic volcanics, Ordovician and Silurian sandstones, shales, and graywackes intercalated with basic volcanics, and Devonian graywackes, conglomerates, and fossiliferous limestones intercalated with basaltic lavas (Buriánek et al., 2022; Soejono et al., 2018). The Gobi-Altai domain consists of Upper Cambrian graywackes, shales, quartz sandstones, and abundant basic tuffs and volcanics, Ordovician graywackes, sandstones, and fossiliferous shales and limestones intercalated with basaltic and felsic volcanics, Silurian fossiliferous shales, sandstones, conglomerates, and limestone, and Devonian graywackes, conglomerates, and fossiliferous shale and limestone beds of variable thickness associated with basic volcanism (Buriánek et al., 2022; Lehmann et al., 2010; Rauzer et al., 1987). Apart from the Upper Cambrian sequences, which are metamorphosed at greenschist-facies conditions, the Ordovician to Devonian strata are not metamorphosed at either the northern or southern flanks of the Altai range. The age of the stratigraphic sequences is well constrained by U-Pb isotopic studies on detrital zircon (Jiang et al., 2012, 2017; Soejono et al., 2018) and by paleontological studies (Budil et al., 2008; Filippova et al., 1990; Markova & Sharkova, 1977; Rauzer et al., 1987). In contrast, the Bodonch-Tseel domain is characterized by high-grade metamorphism, and therefore, its stratigraphy could not have been defined by fossils. It consists of migmatized paragneiss, orthogneiss alternating with numerous amphibolite layers, all intruded by late Devonian and Permian granitoids (Burenjargal et al., 2014, 2016; Hanžl et al., 2016). This domain was previously interpreted as an active continental margin represented by a Precambrian basement metamorphosed during Paleozoic orogeny (Badarch et al., 2002). However, recent U-Pb detrital zircon isotopic studies place the deposition of the Bodonch-Tseel domain gneiss protoliths in the Cambrian to Ordovician (Jiang et al., 2012, 2017).

The Mongolian and Chinese Altai zones were affected by three distinct metamorphic events. The earliest is Barrovian-type metamorphism ranging from a chlorite to kyanite-sillimanite zone interpreted as a result of burial associated with the crustal thickening (e.g., Jiang et al., 2015, 2019; Soejono et al., 2021; Wei et al., 2007; Zorigtkhuu et al., 2011). The age of this metamorphic event was estimated to be late Ordovician in the Hovd domain (*ca*. 455 Ma; Soejono et al., 2021), Silurian in the Bodonch-Tseel domain (*ca.* 450–400 Ma; Burenjargal et al., 2014), and earlier than mid-Devonian in the Chinese Altai Zone (*ca.* 394 Ma; Xu et al., 2021). The second metamorphic event is related to Buchan-type sillimanite and cordierite assemblages (Broussolle et al., 2015; Jiang et al., 2015) in migmatites, interpreted as a result of crustal-scale anatexis associated with regional extension (e.g., Hanžl et al., 2016; Jiang et al., 2019). It occurred at *ca.* 410–380 Ma in the Chinese Altai Zone (Cai et al., 2011; Jiang et al., 2010; M. Sun et al., 2009) and *ca*. 400–370 Ma in the Mongolian Altai Zone (Bibikova et al., 1992; Burenjargal et al., 2014; Hanžl et al., 2016; Kozakov et al., 2002, 2011, 2019). This

metamorphic phase is associated with magmatism, and its volcanic equivalents were dated to *ca*. 400–370 Ma (Demoux et al., 2009; Jiang et al., 2019; Kozakov et al., 2007; J. Zhang et al., 2015). The late Devonian–early Carboniferous (*ca*. 365–340 Ma) metamorphic event was attributed to the upright folding and/or doming of a hot crust (e.g., Kozakov et al., 2019; Lehmann et al., 2017; Soejono et al., 2021; S. Wang et al., 2021). The third tectono-thermal event affecting the southern part of the Altai Zone is represented by important early Permian magmatism (Broussolle et al., 2019; Kozakov et al., 2007; Yarmolyuk et al., 2008). The Permian A-to S-type granitoids (*ca.* 290–250 Ma) not only show alkaline composition and often appear in circular shapes, but also lack deformation, thus they are considered to represent post-tectonic within-plate magmatism (Y. Tong et al., 2014 and references therein; Yarmolyuk et al., 2008). This magmatism is accompanied by intrusions of undeformed gabbros dated at *ca.* 300–270 Ma (Broussolle et al., 2018; C. L. Zhang et al., 2014) and pegmatite vein swarms dated at *ca*. 281–260 Ma (Jiang et al., 2019). The Permian magmatism is also associated with partial melting and high temperature to ultra-high temperature metamorphism dated at *ca*. 300–260 Ma, and can be identified in particular in the southern part of the Chinese Altai Zone (Briggs et al., 2007; Broussolle et al., 2018; Kozakov et al., 2011; Kröner et al., 2010; L. X. Tong et al., 2013).

3. Lithological, Structural, and Metamorphic Characterization of Tectonic Domains

To constrain the internal structure and tectonic evolution of the studied area, detailed lithological and structural studies, along with petrological descriptions of the metamorphic assemblages related to individual fabrics, were carried out for three distinct domains separated by regional shear zones along the N-S trending section. In agreement with the subdivision of the Mongolian Altai tectonostratigraphic scheme of Tomurtogoo (2017), the three domains correspond to principal lithotectonic units of the Mongolian Altai Zone as follows: (a) the Northern domain (ND) can be tentatively correlated to the easternmost extremity of the Hovd domain, and the (b) Central domain (CD) and (c) Southern domain (SD) are attributed by Tomurtogoo (2017) to the Bodonch-Tseel domain (Figure 1, lower left inset). Each individual domain is characterized by unique lithology and/or unique structural and metamorphic records. In the following sections, the lithological, structural, and metamorphic observations for each domain are described from north to south.

3.1. Lithological Characterization

The ND is limited in the north by undeformed gabbros and granitoids of the Lake Zone and in the southeast by the NE-SW trending Bugat fault (Figure 1). In the north, a narrow belt of highly sheared chlorite-muscovite slate (metatuffs), quartzite, and marble occurs (Figure 2a). This sequence is followed by garnet and garnet-staurolite-kyanite micaschist (Figure 2b), terminated by a wide area of migmatitic garnet-sillimanite paragneiss (Figure 2c) and stromatic migmatite (Figure 2d). The micaschists include layers of coarse-grained marble and gneissified porphyritic biotite granitoids, whereas the migmatite is intercalated with amphibolite layers and is intruded by granitoids that form a network of sills, dykes, and locally several-kilometers-wide sheeted plutons (Figures 2c, 2e, 2f).

The CD is a triangular region progressively attenuating to the west. It is limited by the Bugat fault in the north and by an irregular E-W trending sharp boundary with the migmatitic and granitic SD in the south (Figure 1). In the north, low-grade biotite schist intercalated with marble occurs, progressively passing to garnet micaschist, metagraywacke, and quartzite to the south (Figure 2g).

The SD occurs in the footwall of the CD and is separated by a major greenschist-facies shear zone from the southerly Trans-Altai Zone (Figure 1). It is predominantly composed of dark migmatitic augen-gneiss and felsic migmatite associated with anatectic granite (Figures 2h–2k). The dark augen-gneiss has in places metaigneous appearance, with macroscopically euhedral plagioclase phenocrysts and contains xenoliths of metasandstone (Figure 2l). In other places, the dark augen-gneiss has a metasedimentary appearance, with rounded plagioclase clasts and layering defined by variations of grain size and composition. The felsic migmatites are represented by biotite-sillimanite stromatite and biotite nebulite. The characteristic lithology is pearl gneiss and/or ophthalmic migmatite.

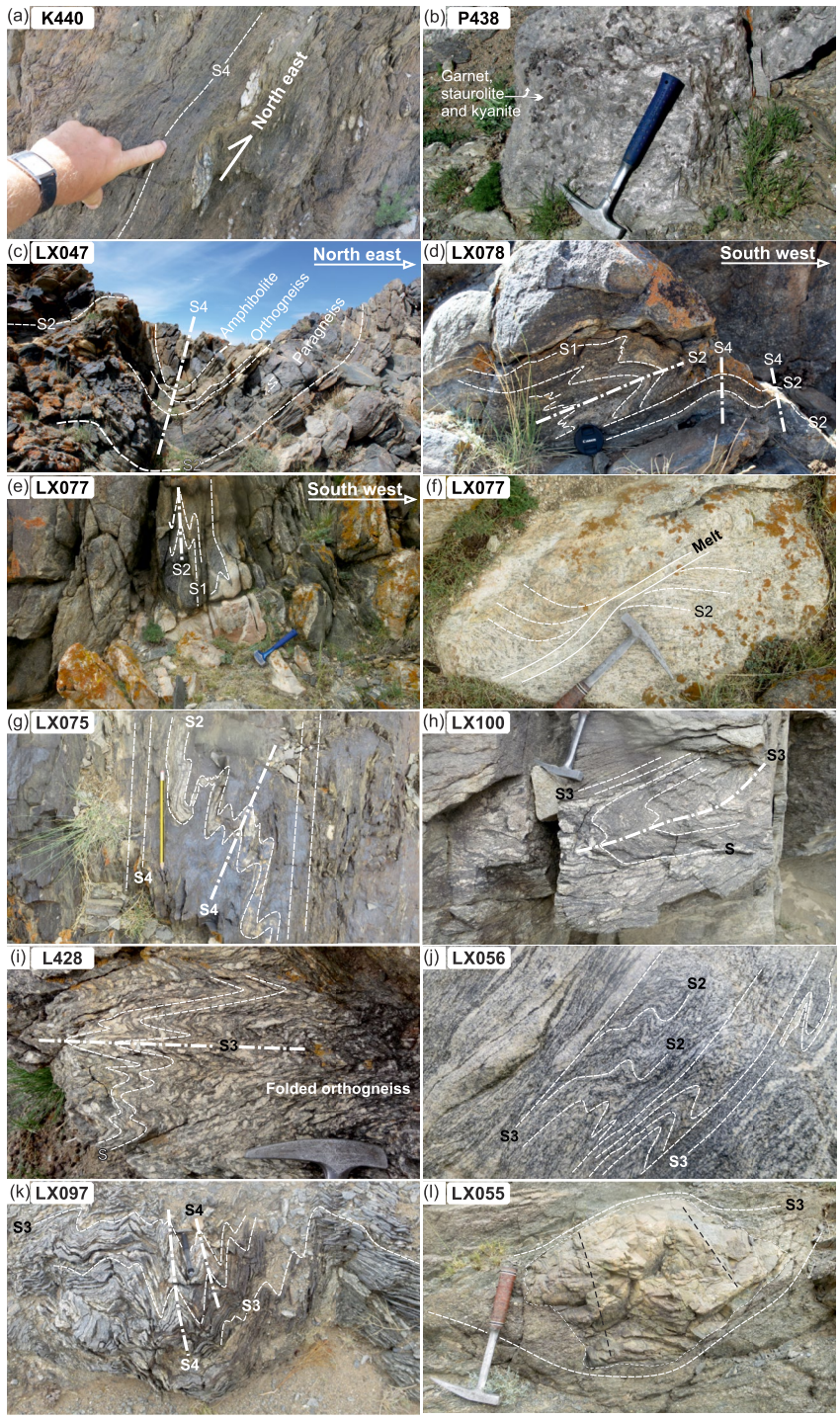

Figure 2.

3.2. Structural and Metamorphic Record

The ND is characterized by ubiquitous NW or SE dipping S2 metamorphic schistosity (Figure 3 and cross-section A in Figure 4). The metasediments of all grades contain relics of S1 foliation in the form of isoclinal folds or cleavage lithons (Figure 2d). The relics of this foliation are possibly also preserved in garnet and staurolite porphyroblasts as inclusion trails (Figures 5a and 5b). However, no relics of S1 fabric were found in the meta-granites. The gneissified granites in the northern part do not show partial melting features, which are typical for

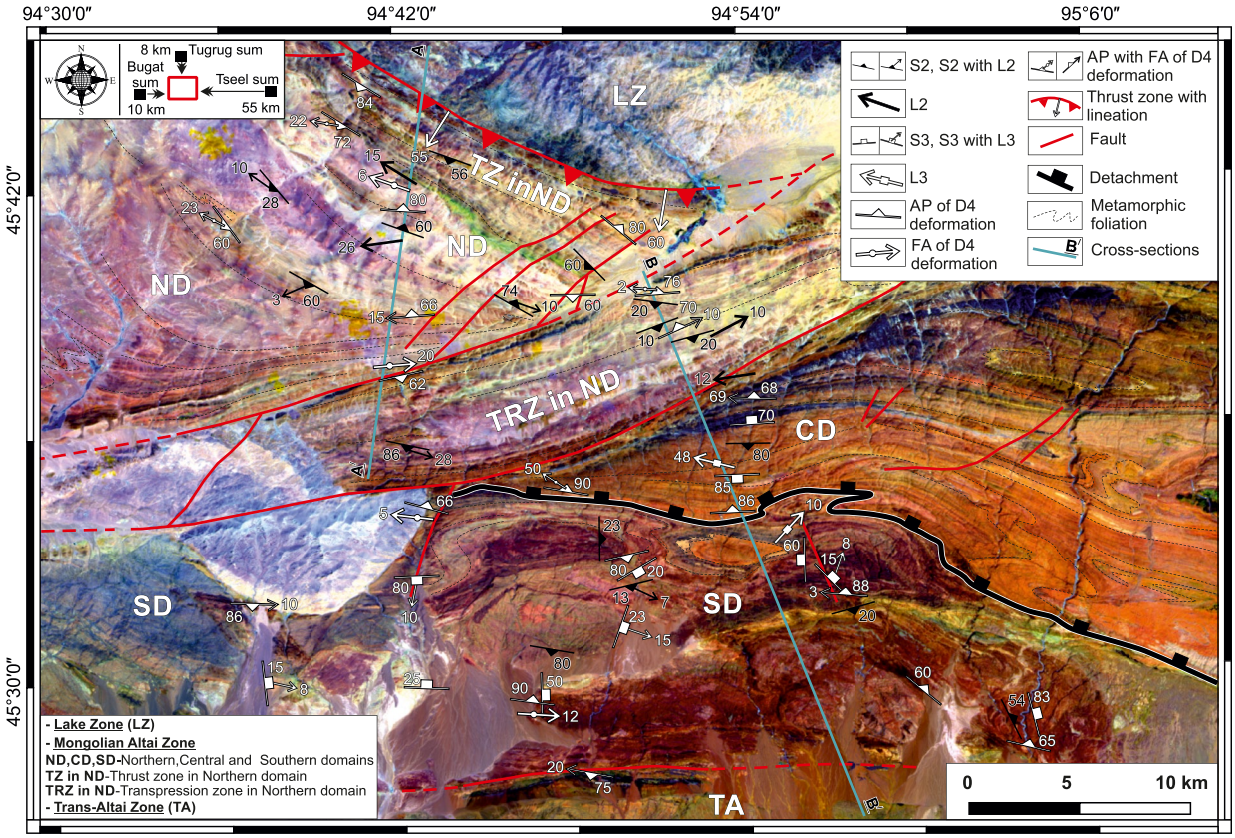

Figure 3. Principal structural features and domain boundaries shown on the enhanced Sentinel-2 map (RGB composite of band ratios 12/2, 11/2, 8/2). The map coverage corresponds to the geological map shown in Figure 1.

granite sheets that intruded the migmatites in the south. In the south, the S2 fabric is represented by stromatitic layering in migmatitic paragneiss and gneissosity in metagranitoids (Figures 2e and 2f). The S2 foliation is underlined by synfolial growth of sillimanite or post-D2 growth of andalusite porphyroblasts and muscovite plates (Figures 5c and 5d). Consequently, the granite sheets are interpreted as being syntectonically emplaced during D2 and in different crustal levels along the M2 metamorphic gradient. The entire sequence is refolded by upright NW-SE trending F4 folds associated with NE-SW striking axial planar greenschist facies cleavage S4 (Figures 2a, 2c, and 3). This deformation reveals a strong gradient marked by a high strain zone related to D4 thrusting of the ND over the weakly deformed Lake Zone in the north (TZ in Figures 1 and 3). The other sharp deformation gradient coincides with a zone of sinistral transpression where the S2 fabric is reoriented to NE-SW and transposed by S4 greenschist-facies foliation (Figures 1 and 3). This zone was intruded by the Triassic Ulaan Undur granite (*ca*. 211 Ma; Cai et al., 2015) and later reactivated by the Bugat fault with sinistral offset of up to 8 km (Figures 1 and 3). The fold hinges of the F4 folds are generally sub-horizontal, implying that the S2 fabric

Figure 2. Field photographs showing the main rock types and structural relationships observed in the studied area along the NNW-SSE profile. In the Northern domain (ND): (a) sub-vertical S4 foliation in the low-grade mu-chl-bearing slate located within the thrust zone (TZ in the ND); (b) Barrovian-type mica-schist with porphyroblasts of garnet, staurolite, and kyanite located in the central part; (c) open F4 folds in an amphibolite, orthogneiss, and paragneiss sequence affecting the main sub-horizontal S2 foliation in the southernmost part; (d) remnants of S1 foliation folded and locally transposed into the S2 axial plane in the partially molten migmatitic paragneiss and refolded by open F4 folds located within the transpression zone (TRZ in the ND); (e) coarse-grained leucogranite vein emplaced parallel to S1 foliation and folded by F2 folds that folded and transposed the previous S1 foliation within the TRZ; and (f) extensional D1 shear band developed in the migmatitic orthogneiss within the TRZ. In the Central domain (CD): (g) sub-horizontal S2 foliation folded by asymmetric F4 folds and transposed into vertical S4 axial planar cleavages in the medium-grade metagraywacke located in the northernmost part. In the Southern domain (SD): (h) migmatitic S2 fabric reworked and transposed by the late or mylonitic metamorphic S3 fabric; (i) high-grade metamorphic S2 fabric folded by tight and asymmetric F3 folds in a gneissic granite; (j) high-grade migmatitic S2 fabric reworked by the subsequent D3 deformation under high-grade conditions; (k) high-grade, highly mylonitized metamorphic fabric (S3) folded during late deformation (D4); and (l) fine-grained quartzite with a bedding layer or metamorphic foliation (outlined by a black dashed line) enclosed within the higher-grade mylonitic fabric (S3).

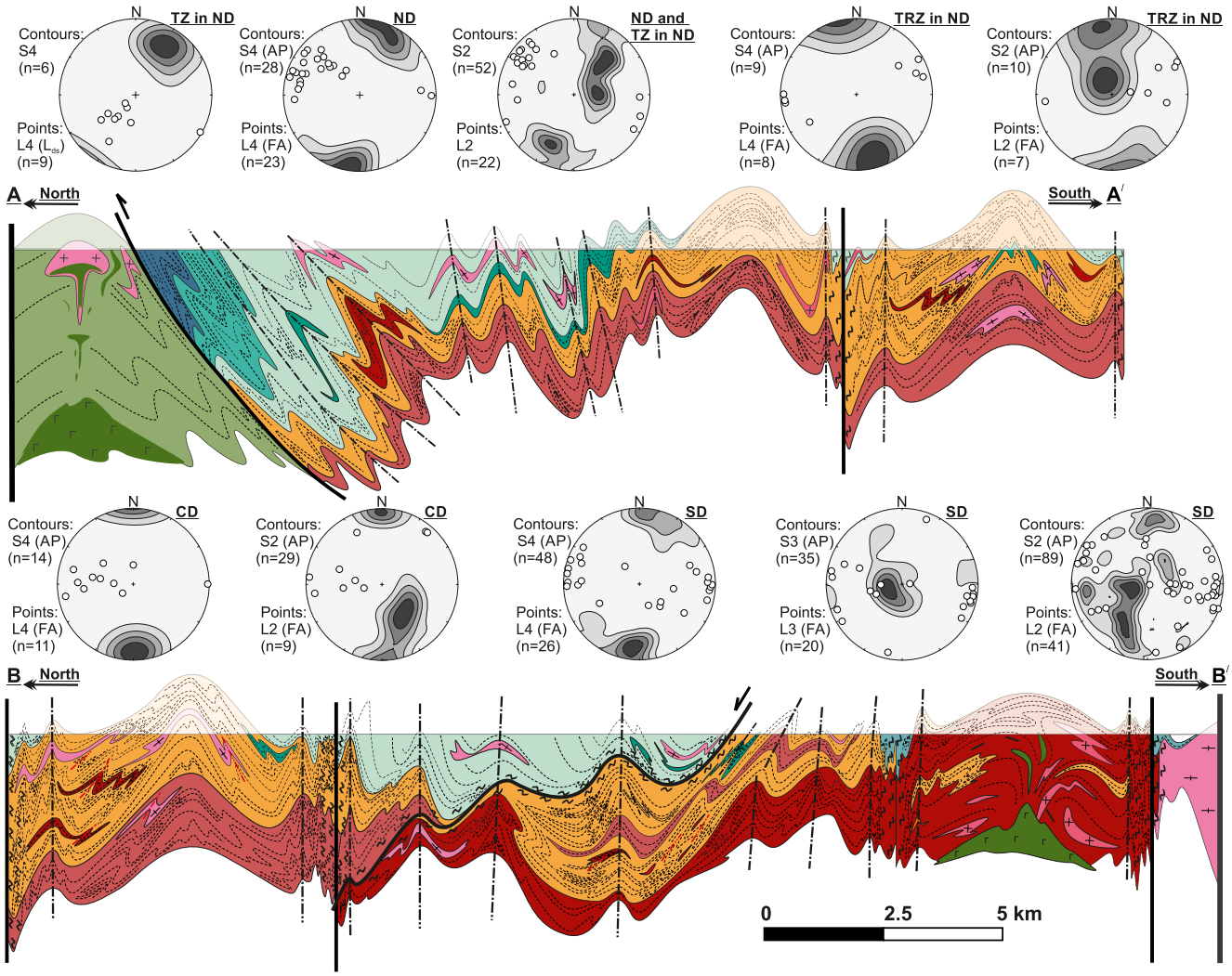

Figure 4. Structural profiles across the studied area, showing the principal structural features. The stereonets show the orientation of major structural elements (S2, S3, and S4 planar structures, mostly foliations and axial planar cleavages [AP] - contours, L2, L3, and L4 linear structures, mostly stretching lineations and fold axes [FA] - points). For the legend of the cross-section, see Figure 1. Line styles in -sections follow the legend from Figure 1.

was also originally sub-horizontal (Figures 3 and 4). The only exception is the northern thrust zone, where strong dip-slip L4 stretching lineation confirms the general NNE-SSW-oriented D4 shortening (Figures 3 and 4).

The CD is featured by steep fabrics with E-W orientation, attributed to important D4 shortening (Figures 3 and 4). However, the main metamorphic foliation is represented by S2 amphibolite-facies schistosity, which is axial planar to isoclinal kilometer-scale F2 folds that deform S1 compositional layering (Figure 5e). The F2 folds show steeply to gently east plunging axes that are parallel to the principal L2 intersection and stretching lineation (Figures 3 and 4). Metamorphic grade related to S2 foliation ranges from biotite zone in the north to garnet zone in the south. The whole domain is heterogeneously reworked by D4 deformation producing upright F4 folds with sub-horizontal hinges and sub-vertical E-W trending greenschist-facies axial planar cleavage (Figures 2g and 3). Like in the ND, the intensity of the D4 deformation increases toward domain boundaries, where zones of D4 fabric transposition occur.

The principal feature of the SD is the existence of dominant subhorizontal S3 fabric (Figures 2h–2j), which is missing in the CD and ND (Figure 3). The metamorphic conditions of this fabric range from sillimanite-cordierite-bearing migmatitic layering to greenschist-facies mylonitic foliation (Figures 5f–5h). Nevertheless, the relics of variably SSW- or NNE-dipping S2 fabric are preserved in rare low strain domains; for example, in the less-competent stromatitic migmatites where the S2 foliation is folded by isoclinal flow folds F3 (Figures 2h–2j) and mainly in

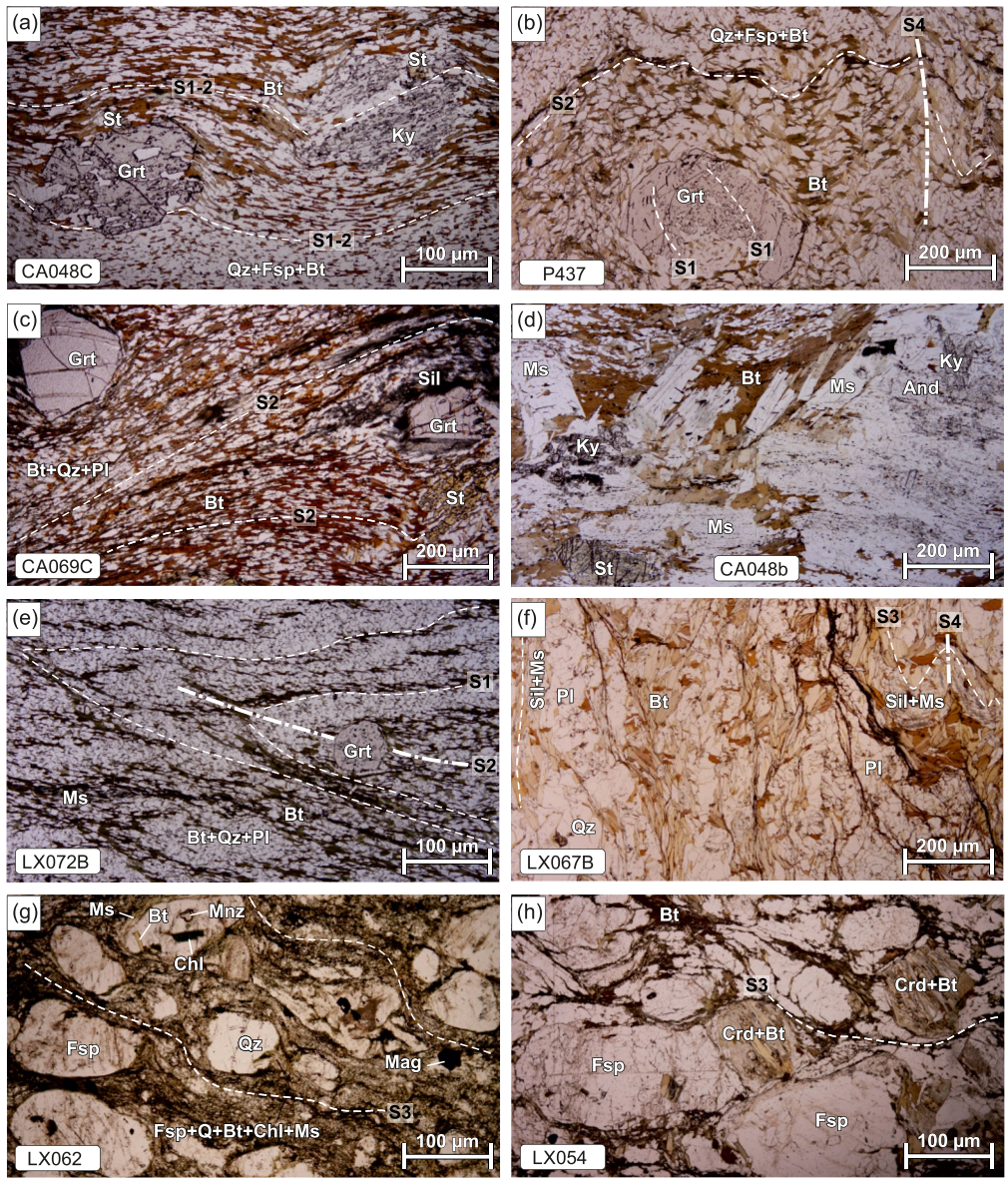

Figure 5. Microphotographs of mineral assemblages and microstructural relations of the most representative metamorphic rocks from the three distinct domains of the studied area. (a–d) Barrovian-type schists from the ND: (a) garnet and kyanite poikiloblasts including a straight S1 internal foliation defined by quartz and ilmenite, continuous with the external composite S1–2 foliation and without pressure shadows, suggesting an intense transposition of S1 into S2 fabric; (b) garnet porphyroblast with inclusion trails of ilmenite and quartz parallel to S1 foliation and oriented at a high angle to the external S2 foliation. The external S2 foliation is defined by oriented biotite and ilmenite and is refolded by the late D4 deformation event; (c) garnet and staurolite porphyroblasts in a matrix dominated by fibrolitic sillimanite and biotite parallel to S2 foliation; and (d) kyanite replaced by andalusite and surrounded by platy muscovite. (e) Garnet-bearing micaschist from the CD with metamorphic S2 foliation defined by alternating quartz-plagioclase-rich layers and biotite-rich layers folded and transposed into the S3 axial planar cleavage marked by biotite. (f–h) Garnet-sillimanite bearing paragneiss and mylonitized metagranodiorite rocks from the SD: (f) high-grade metamorphic S3 fabric defined by biotite and fibrolitic sillimanite and folded by late F4 folds associated with crystallization of platy muscovite; (g) highly mylonitized metagranodioirite with coarse-grained quartz and feldspar enclosed in a fine-grained matrix of oriented feldspar, quartz, biotite, chlorite, and muscovite parallel to S3; and (h) moderately gneissified and gneissic metagranodioirite with coarse-grained feldspar, quartz, and pinnitized cordierite surrounded by oriented biotite parallel to S3. Mineral abbreviations are after Whitney and Evans (2010).

Table 1
General Description and Mineral Assemblage of the Analyzed and/or Dated Samples From the Studied Area

Sample	Longitude	Latitude	Sample name	Mineral assemblage[a]	Methodology		
					WR geochemistry	U-Pb dating	Zircon-Hf isotope
Lake Zone (LZ)							
LX089	94.6895	45.7672	Metagranite	Kfs-qz-pl ± amp-bt-chl-opq	√	√	√
Mongolian Altai Zone							
Northern Domain (ND)							
CT006	94.6884	45.7465	Quartzitic sandstone	Qz ± pl-chl-bt	√	√	√
CT002A	94.7248	47.7143	Metasandstone	Qz-pl-kfs-bt-ms-chl-opq ± ep	√	√	
LX086	94.6962	45.7197	Metagreywacke	Pl-bt-q-ms	√	√	√
CT001	94.704025	45.707027	Metasandstone	Qz-kfs-pl-ms-bt-chl-opq	√		
LX081	94.7	45.6268	Metagranite	Kfs-qz-pl-ms	√	√	
LX078	94.86364	45.640427	Metagranite	Kfs-pl-qz-ms ± grt	√		
LX077	94.8713	45.6372	Granite vein	Kfs-pl-qz-bt-ms-chl ± ep-amp	√	√	√
Central Domain (CD)							
LX076	94.8945	45.6205	Metagreywacke	Qz-pl-bt-ms-cal-[chl]	√	√	√
LX074	94.9048	45.6011	Metagreywacke	Qz-pl-bt-ms-[chl]	√	√	√
LX072A	94.8954	45.5804	Micaschist	Qz-pl-bt-grt-ms-[chl]		√	
Southern Domain (SD)							
LX067B	94.9334	45.5592	Paragneiss	Pl-qz-bt-ms-sil-crd-chl		√	
LX063	94.9501	45.5348	Metagranodiorite	Pl-kfs-qz-bt-chl-ms-ep-mnz		√	
LX062	94.9562	45.5309	Metagranodiorite	Pl-kfs-qz-bt-chl-ms-mnz	√	√	√
CT005	95.0001	45.4911	Metasandstone	Qz-pl-bt-ms-chl	√	√	√
LX056	95.0574	45.4783	Metagranodiorite	Pl-kfs-qz-bt-chl-ms-mag	√	√	√

Note. Sample localities are shown in Figure 1.

[a]Mineral abbreviations used are: pl, plagioclase, ksp, K-feldspar, qz, quartz, bt, biotite, amp, amphibolite, crd, cordierite, sil, sillimanite, grt, garnet, ep, epidote, mnz, monazite, mag, magnetite, opq, opaque mineral, chl, chlorite, cal, calcite (Whitney & Evans, 2010).

the incompetent metasandstone xenoliths surrounded by homogeneously foliated metaigneous rocks (Figure 2l). Here, the S2 occurs at a high angle to the ubiquitous S3 foliation (see stereoplots in Figure 4). The main argument for the distinction of the S2 foliation is its migmatitic character similar to that observed in the southern part of the ND. The entire domain is folded by WNW-ESE trending F4 upright folds (Figures 2k and 3), producing large-scale brachyantiforms cored by dark augen-gneiss and brachysynforms cored by migmatites and micaschists (Figures 1 and 3). The central part of this domain is diagonally crosscut by a zone of intense D4 deformation along which the low-grade cover rocks are juxtaposed to the migmatitic and igneous lithologies. This zone is also associated with important greenschist-facies WNW-ESE striking cleavage (Figure 3) and upright, close-to-isoclinal F4 folds developed at all scales (Figure 5f).

4. Whole-Rock Geochemistry

Whole-rock major and trace element analyses were carried out on seven metasedimentary and six magmatic rock samples each 5–10 kg in weight (see Figure 1 for sample locations); some of these samples were further studied by U-Pb and Hf-isotope zircon geochronology. The GPS locations, general descriptions, and mineral assemblages are summarized in Table 1.

After crushing and homogenization of samples using an agate mill at the Central Geological Laboratory in Ulaanbaatar (Mongolia), the resultant powders were analyzed at both the Activation Laboratories Ltd. (Actlabs) and Bureau Veritas Mineral Laboratories in Vancouver, BC, Canada. At Actlabs, three sedimentary samples and one magmatic sample were analyzed, using the 4Lithoresearch procedure (http://www.actlabs.com), and

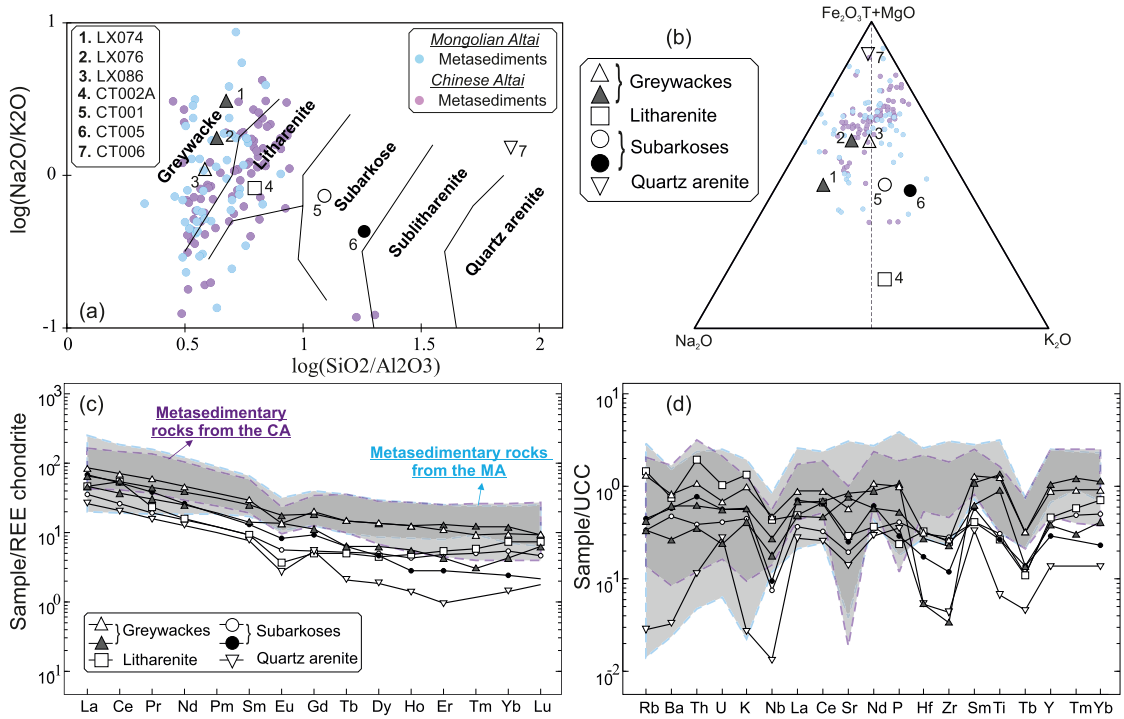

Figure 6. Geochemical characterization diagrams for the metasedimentary rocks collected along the NNW-SSE profile of the Mongolian Altai Zone: (a) classification diagram after Pettijohn et al. (1972); (b) Na_2O-K_2O-(Fe_2O_3t + MgO) ternary diagram after Blatt et al. (1972); (c) chondrite-normalized rare-earth element (REE) patterns (Boynton, 1984); and (d) upper continental crust (UCC)-normalized trace element patterns (Taylor & McClennan, 1985). Symbols: open/white for samples from the Northern domain (ND), gray for the Central domain (CD), and black for the Southern domain (SD). For comparison, literature on chemical data of metasedimentary rocks from the Mongolian Altai Zone (Burenjargal et al., 2014; Jiang et al., 2012, 2017; Soejono et al., 2017; Sukhorukov et al., 2016) and Chinese Altai Zone (B. Chen & Jahn, 2002; Hu et al., 2000; Long et al., 2008, 2012; Sun et al., 2008; Y. Wang et al., 2014) are shown.

major-element concentrations were obtained by inductively coupled plasma-optical emission spectrometry and trace-element concentrations by inductively coupled plasma-mass spectrometry, following lithium metaborate/tetraborate fusion and weak nitric acid dissolution. For the remaining samples, four sedimentary and five magmatic rocks, whole-rock analyses were carried out using X-ray fluorescence (major and minor elements, code XF700) and lithium borate fusion inductively coupled plasma-emission spectrometer/mass spectrometer (Ultra Trace, code MA250) in the Bureau Veritas Mineral Laboratories (https://www.bvna.com/sites/g/files/zypfnx386/files/media/document/Bureau-Veritas-CAD-Fee-Schedule-2022.pdf). The analyses from the metasedimentary and magmatic rocks are shown in Appendix A of the Supporting Information (Tables A1 and A2 in Supporting Information S1, respectively).

For the metasedimentary rocks, major-element analyses are presented in a series of classification diagrams showing the graywacke-dominated nature (Blatt et al., 1972; Pettijohn et al., 1972) and the trace-element analyses are shown in spider plots normalized to chondrite (Boynton., 1984) and upper continental crust (UCC; Taylor & McClennan, 1985) in Figure 6. For the magmatic rocks, the major-element analyses are plotted in two classification diagrams (Cox et al., 1979; Irvine & Baragar, 1971), and the trace-element analyses are presented in spider plots normalized to chondrite (Boynton, 1984) and typical mid-ocean ridge basalt (S. S. Sun & McDonough, 1989) in Figure 7. The geochemical data are plotted using the GCDkit 6.0 package (Janoušek et al., 2006), in which published geochemical analyses from other metasedimentary and magmatic rocks of both the Mongolian and Chinese Altai zones are also presented for comparison.

4.1. Metasedimentary Rocks

The geochemical analyses of metasedimentary rocks were obtained for four samples (CT006, CT002A, LX086, and CT001) collected in the ND, two samples (LX076 and LX074) from the CD and one sample (CT005) from the SD (Figure 1 and Table 1). The geochemical compositions of samples from all domains vary widely, with

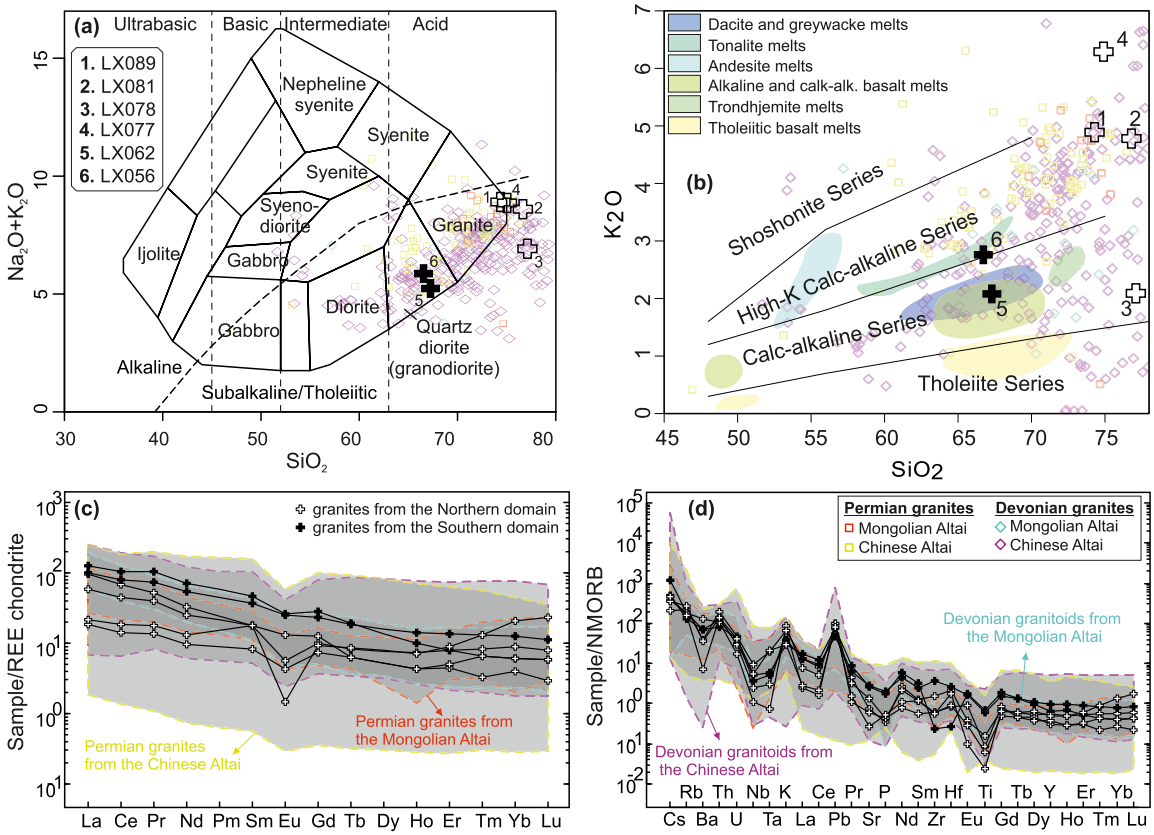

Figure 7. Geochemical characterization diagrams for granitoids collected along to the NNW-SSE profile of the Mongolian Altai Zone: (a) TAS ($Na_2O + K_2O$ vs. SiO_2 in mol.%) diagram (Cox et al., 1979) with black dashed lines denoting the boundary between alkaline and subalkaline rocks according to Irvine and Baragar (1971); (b) binary SiO_2–K_2O plot with the discrimination boundaries between the tholeiitic, calc-alkaline, high-K calc-alkaline, and shoshonitic rocks of Peccerillo and Taylor (1976). The fields of experimental melts derived from various sources are taken from Figure 3 of Roberts and Clemens (1993); (c) chondrite-normalized REE patterns (Boynton, 1984); and (d) normal mid-ocean ridge basalt (NMORB) normalized spider plots (Sun & McDonough, 1989). For comparison, literature on chemical data of Devonian granitic rocks from both the Mongolian Altai Zone (Hanžl et al., 2016; Helo et al., 2006; Jiang et al., 2012) and Chinese Altai Zone (Cai et al., 2012; Chai et al., 2009; B. Chen & Jahn, 2002; Cui et al., 2020; Lin et al., 2019; Sun et al., 2008; Tong et al., 2007; T. Wang et al., 2006, Y. Wang et al., 2011; Yang et al., 2010; Yu et al., 2017; Yuan et al., 2007; C. Zhang et al., 2017; H. Zhang et al., 2003; Z. Zhang et al., 2006) and Permian granitic rocks from the Mongolian Altai Zone (Burenjargal et al., 2016; Helo et al., 2006) and Chinese Altai Zone (Briggs et al., 2007; F. P. Gao et al., 2010; Li et al., 2004; Tong et al., 2014, 2006; C. L. Zhang et al., 2010, 2012; Zhou, Zhang, Luo, et al., 2007; Zhou, Zhang, Wang, 2007) are shown.

SiO_2 = 63.0–93.9 wt.%, Al_2O_3 = 1.24–16.4 wt.%, and Fe_2O_3t + MgO = 1.48–10.04 wt.%. The CaO, Na_2O, and K_2O vary from 0.09 to 4.38 wt.% (see Table A1 in Supporting Information S1). In the log(Na_2O/K_2O) vs. log(SiO_2/Al_2O_3) diagram (Figure 6a), the metasedimentary rocks depict a decreasing trend in Al_2O_3 with increasing SiO_2, and SiO_2/Al_2O_3 ratios range from 3.8 to 75.7; therefore, these samples are classified as graywackes (LX086, LX076, and LX074; triangle), litharenite (CT002A; square), subarkoses (CT001 and CT005; circle), and quartz arenite (CT006; reverse triangle) in the diagram of Pettijohn et al. (1972; Figure 6a). In the Fe_2O_3t + MgO–Na_2O–K_2O ternary diagram (Figure 6b), the graywackes and quartz arenite fall in the sodic sandstone field, while litharenite and subarkose are clustered in the potassic sandstone field. However, the quartz arenite appears closer to the ferromagnesian corner in comparison with graywackes. As a whole, the metasedimentary rocks from all domains can be divided into three distinct groups according to the observed compositions: sodic sandstone (graywackes), potassic sandstone (litharenite-subarkose), and ferromagnesian sodic sandstone (quartz-arenite).

The rare-earth element (REE) abundances for the graywackes, litharenite-subarkose, and quartz arenite are variable (ΣREE = 38–140 ppm; Table A1 in Supporting Information S1), showing higher REE contents in graywackes (74–140 ppm) and lower REE contents in quartz arenite (38 ppm). Despite the differences in REE abundances, all samples show moderate light rare-earth element (LREE) enrichment with respect to heavy rare-earth element (HREE) and relatively flat to concave HREE patterns, indicating REE fractionation (Figure 6c). In addition, moderate to weak negative Eu-anomalies (Eu/Eu* = 0.42–0.82; Figure 6c and Table A1 in Supporting

Information S1) can be also observed in all samples except for one graywacke sample (LX074), which displays a slightly positive Eu anomaly (Eu/Eu* = 1.07). In general, the REE compositional ranges of graywackes overlap the metasedimentary group from the Chinese and Mongolian Altai zones, whereas the litharenite-subarkose and quartz arenite samples show lower concentrations of HREE in comparison with all the analyzed rocks from the Chinese and Mongolian Altai zones. In the UCC multi-element diagram (Figure 6d), both the graywacke and litharenite-subarkose samples show similar patterns apart from the quartz arenite. All samples are characterized by depletion in high field strength elements (HFSE), such as Nb, Hf, Zr, and Tb, and moderate depletion in Sr. Significant enrichment of some large-ion lithophile elements (LILE), such as Rb and K, can be observed in the graywackes and litharenite-subarkose, whereas moderate enrichment of Sm can be depicted in all samples. These patterns resemble sediments from the Chinese and Mongolian Altai zones, but show lower concentrations of some HFSE (e.g., in Zr, Hf, Nb, Tb, Y, Tm, and Yb).

4.2. Magmatic Rocks

The analyzed magmatic rocks include a weakly gneissified granite from the Lake Zone (LX089), two metagranite samples and a granite vein from the ND (LX081, LX078, and LX077), and two variously deformed metagranodiorites from the SD (LX062 and LX056; Figure 1 and Table 1). The samples from the Lake Zone and ND (LX089, LX081, LX078, and LX077) show high SiO_2 content (74.29–77.10 wt.%) and low contents of Al_2O_3 (12.9–13.9 wt.%), Fe_2O_3 (0.8–1.3 wt.%), MgO (0.16–0.25 wt.%), and CaO (0.44–1.15 wt.%) with respect to the samples from the SD (Table A2 in Supporting Information S1). The Na_2O and K_2O contents range from 3.21 to 4.71 wt.% and from 2.08 to 4.89 wt.% in all the samples, except for the granite vein (LX077) which shows lower Na_2O content (2.61 wt.%) and higher K_2O content (6.29 wt.%). All studied granitic samples have low loss-on-ignition content (LOI = 0.1–0.9 wt.%; Table A2 in Supporting Information S1). The $Na_2O + K_2O$ content varies from 6.80 to 8.96 wt.% in all the metagranitic and granite vein samples from the Lake Zone and ND, whereas the metagranodiorite samples from the SD have a $Na_2O + K_2O$ (wt.%) content ranging from 5.36 to 5.97 wt.% (Figure 7a and Table A2 in Supporting Information S1). The total alkali-silica (TAS in Figure 7a; Cox et al., 1979) diagram indicates that all the granitic samples have felsic composition and are generally sub-alkaline/tholeiitic according to the dividing line of Irvine and Baragar (1971). The samples from the Lake Zone and ND can be classified as granite, whereas the samples from the SD cluster in the granodiorite field (Figure 7a). The A/CKN ratio (molecular $Al_2O_3/[CaO + Na_2O + K_2O]$) ranges between 1.36 and 1.81 for all samples, indicating a peraluminous character (Table A2 in Supporting Information S1). Based on the binary SiO_2–K_2O diagram of Peccerillo and Taylor (1976) (Figure 7b), most of the samples from the Lake Zone and ND can be represented as a high-K calc-alkaline to shoshonitic series, except for one gneissic granite (LX78) which plots in the calc-alkaline series field. Both metagranodiorite samples of the SD (LX062 and LX056) plot in the calc-alkaline series field. Altogether, the studied granitic rocks overlap and follow the calc-alkaline trend defined by the Devonian and Permian granitic rocks from the Chinese and Mongolian Altai zones (e.g., Broussolle et al., 2019; Burenjargal et al., 2016; Jiang et al., 2016).

Based on the chondrite-normalized multi-element diagram (Figure 7c), the mylonitized metagranodiorite and gneissic metagranodiorite from the SD show higher REE abundance (ΣREE = 171–215 ppm) compared to the samples from the Lake Zone and ND (ΣREE = 34–130 ppm; Table A2 in Supporting Information S1). The REE patterns of the samples from the SD are relatively flat with a slight enrichment in LREE with respect to HREE and without obvious negative Eu anomalies (Eu/Eu* = 0.71–0.84). In contrast, the samples from the Lake Zone and ND show large variations of LREE and HREE contents, displaying a slight to moderate enrichment in LREE with respect to HREE, a marked Eu depletion (Eu/Eu* = 0.11–0.87), and flat to concave HREE patterns except for the granite vein (LX077). The granite vein exhibits moderate LREE enrichment (La_N/Yb_N = 16.4), weak negative Eu anomaly (Eu/Eu* = 0.87), and a slight depletion in HREE (Eu_N/Yb_N = 3.2). On the other hand, the gneissic granite (LX078) from the easternmost part of the ND shows a moderate enrichment in HREE (Eu_N/Yb_N = 0.07), which may be due to the presence of garnet, and a strong negative Eu anomaly (Eu/Eu* = 0.11). The REE patterns of the studied samples are similar to those of granitoids from the Chinese and Mongolian Altai zones; however, they do show marked negative Eu anomalies. In the normal mid-ocean ridge basalt (S. S. Sun & McDonough, 1989) normalized multi-element diagram, nearly all samples have similar characteristics (Figure 7d). Most of them show intense depletion in some HFSE, such as Nb and Ti, and in Ba and Sr. In addition, a high enrichment in LILE (such as Cs, Rb, and K) and in Th and Pb can be also observed (Figure 7d). These samples have patterns resembling Devonian granitoids from both the Mongolian and Chinese Altai zones (purple and light blue dashed lines in Figure 7d).

Table 2
Summary of New U-Pb (LA-ICP-MS) Zircon Ages From This Study Together With All Available U-Pb Zircon Data Reported From the Studied Area

Sample	Rock-type	Ages (Ma)			References
		Depositional	Magmatic	Metamorphic	
LX089	Metagranite	-	371 ± 2.1	-	[This study]
MK78	Granodiorite	-	369 ± 3.0	-	Cai et al. (2015)
CT006	Quartzitic sandstone	475 ± 2.6	-	-	[This study]
CT002A	Metasandstone	438 ± 3.4	-	-	[This study]
LX086	Metagreywacke	446 ± 2.9	-	-	[This study]
LX081	Metagranite	-	278 ± 2.5	-	[This study]
MK83	Massive biotite granite	-	372 ± 3.0	-	Cai et al. (2015)
MK80	Mylonitic granite	-	382 ± 5.0	-	Cai et al. (2015)
LX077	Granite vein	-	362 ± 6.1	-	[This study]
MK81	Syenite	-	211 ± 3.0	-	Cai et al. (2015)
LX076	Metagreywacke	438 ± 1.6	-	-	[This study]
LX074	Metagreywacke	438 ± 1.4	-	278 ± 3.5	[This study]
LX072A	Micaschist	489 ± 5.5	-	-	[This study]
LX067B	Paragneiss		-	271 ± 7.7	[This study]
CT005	Metasandstone	463 ± 3.6	-	-	[This study]
LX063	Metagranodiorite	-	286 ± 1.3	-	[This study]
LX062	Metagranodiorite	-	294 ± 1.3	-	[This study]
LX056	Metagranodiorite	-	296 ± 1.0	-	[This study]

Note. The localities of samples and previous U-Pb zircon data are shown in Figure 1.

5. U-Pb Zircon Dating and Hf Isotopic Signatures

U-Pb dating of zircons was carried out in a batch of 14 samples collected along the NW-SE profile of the Mongolian Altai Zone, from which 9 samples were selected for zircon Lu-Hf isotope analyses (Figure 1). The U-Pb isotopic analyses were performed by laser ablation-inductively coupled plasma mass spectrometry (LA-ICP-MS) at the Czech Geological Survey in Prague (Czech Republic). Details of sample preparation can be found in Appendix B1 in Supporting Information S1, whereas detailed operating conditions and analytical procedures are provided in Appendix B2 in Supporting Information S1. The U-Pb ages are summarized in Table 2 and the original data organized according to the division of the ND, CD, and SD and the rock type are available in Appendix A of the Supporting Information S1 (Tables A3–A7 in Supporting Information S1). All Concordia and Tera-Wassenburg diagrams (Ludwig, 1998), histograms with kernel density estimates (Vermeesch, 2012), and weighted mean diagrams (Ludwig, 2003) were constructed using the statistical software IsoplotR/IsoplotRgui (Github version 1001/639; Vermeesch, 2018). The diagrams were built with highly concordant zircons, between 95% and 105% of concordance, and the errors reported in the text and the diagrams are 2σ (Figures 8 and 10–12).

Zircon Hf isotope analyses were carried out in two different laboratories in several analytical sequences: a *Nu Plasma* HR MC-ICP-MS coupled with a Resonetics RESOlution M-50 laser ablation system (LLC, USA), conducted at the Department of Earth Sciences of the University of Hong Kong; and a *Nu Plasma II* MC-ICP-MS (Wrexham, Wales, UK) equipped with a *RESOlution LR* laser-ablation system (Canberra, Australia), conducted at Nanjing FocuMS Technology Co. Ltd. Details of the analytical procedures can be found in Appendix B3 in Supporting Information S1. Epsilon Hf(t) vs. crystallization age (Ma), as well as T_{DM}^{C} model ages of the zircons, are shown in Figure 9. All data are summarized in Table 3 and the original data are available in Appendix A of Supporting Information (Tables A8 and A9 in Supporting Information S1).

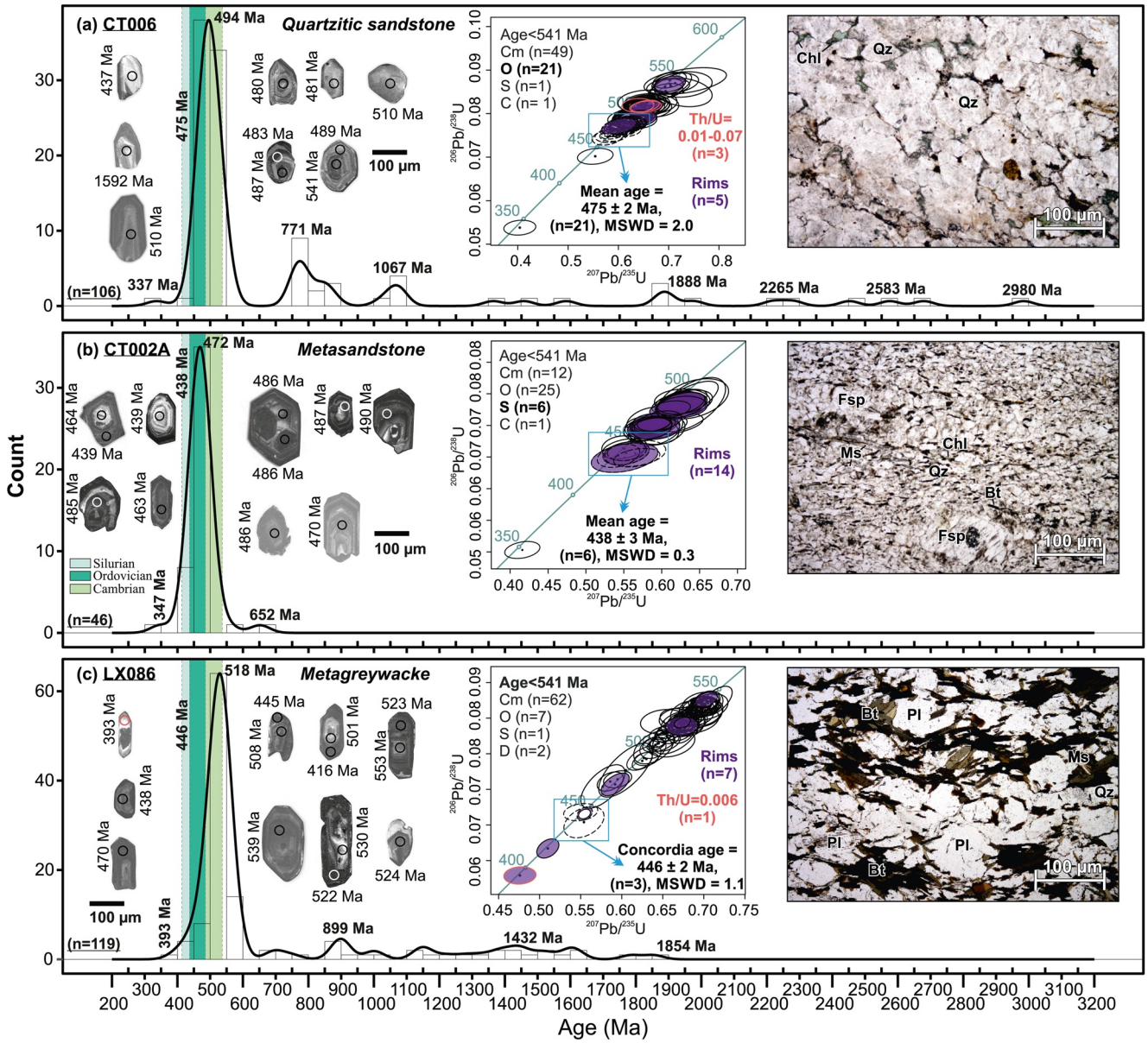

Figure 8. Frequency histogram diagrams with kernel density estimate (KDE) for detrital zircon of samples collected in the Northern domain (ND) of the studied area. The insets show representative cathodoluminescence (CL) images of analyzed zircons, the details of the Concordia age plot, and the microphotographs of the dated samples: (a) medium-grained quartzitic sandstone (CT006) composed of abundant quartz and rare chlorite and biotite; (b) metasandstone (CT002A) with fine-grained quartz, feldspar, biotite, chlorite, and muscovite; and (c) medium-grained metagraywacke (LX086) composed of plagioclase, quartz, biotite and muscovite. Calculated Concordia ages shown in the inset are based on data from the dashed ellipses in blue rectangles. Solid ellipses represent concordant data (>95%) but are not included in the age calculation. Filled ellipses (purple) represent data from the zircon rims, whereas open ellipses represent age data from the cores. All light coral-colored ellipse lines indicate a Th/U ratio <0.1. Only analyses less than 5% discordant are considered. Locations of LA-ICP-MS analysis are shown and the numbers correspond to $^{206}Pb/^{238}U$ ages (<1,000 Ma) and $^{207}Pb/^{206}Pb$ ages (>1,000 Ma). Error bars and error ellipses are 2σ. The age distribution for Silurian, Ordovician, and Cambrian periods is underlined by colors (see legend). For the color version, please refer to the online version.

5.1. Metasedimentary Rocks of the Northern Domain

Zircons from three metasedimentary samples include a quartzitic sandstone (quartz arenite CT006) composed of medium-grained quartz and minor feldspar, biotite, and chlorite (micrograph in Figure 8a); a fine to medium-grained metasandstone (litharenite CT002A) formed by medium-grained elongated quartz and feldspar in a fine-grained matrix defined by recrystallized quartz and plagioclase and oriented biotite and muscovite replaced locally by late chlorite (micrograph in Figure 8b); and a medium-grade and well-foliated metagraywacke

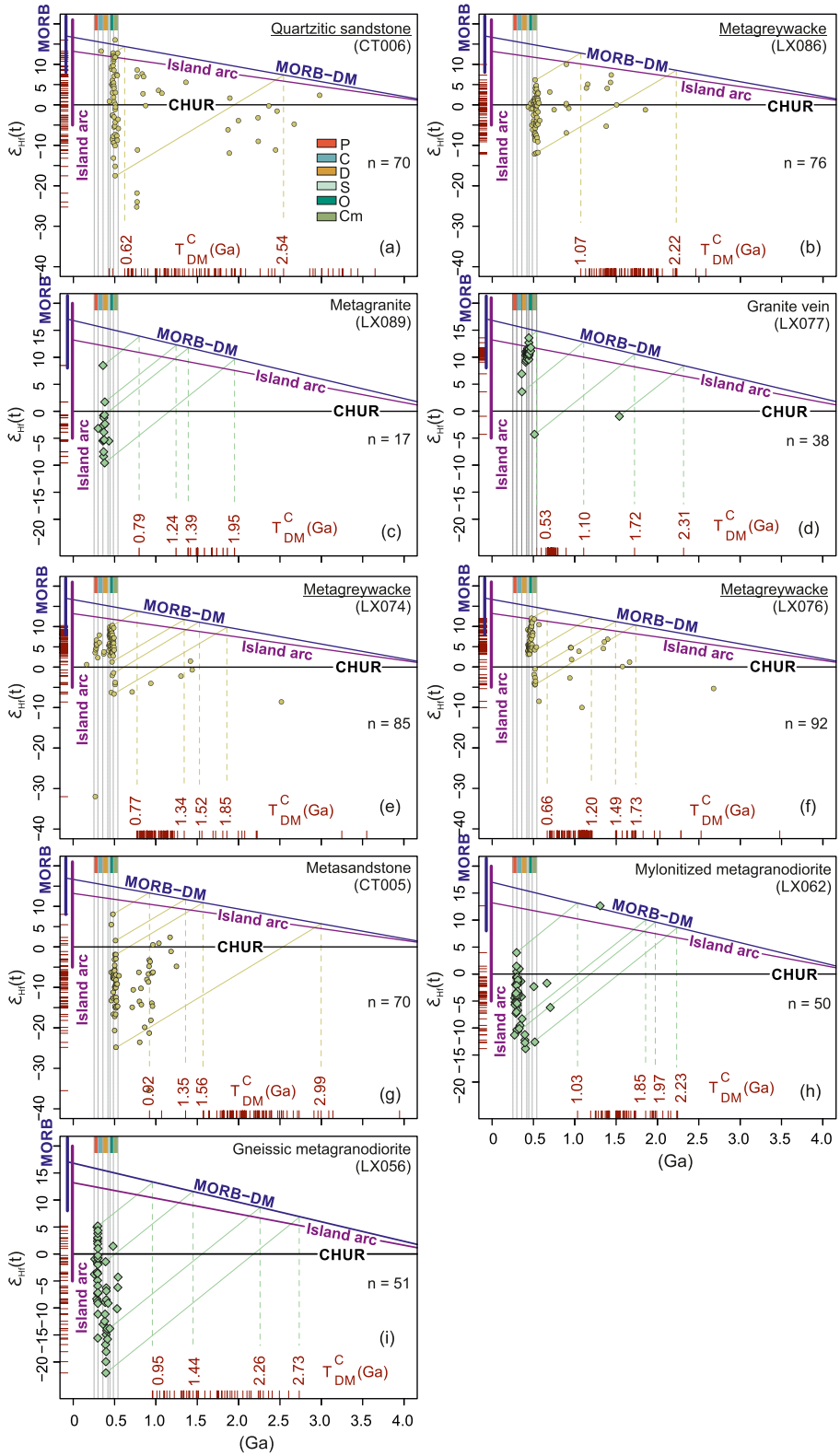
Quartzitic sandstone
(CT006)
n = 70
(a)
Metagreywacke
(LX086)
n = 76
(b)
Metagranite
(LX089)
n = 17
(c)
Granite vein
(LX077)
n = 38
(d)
Metagreywacke
(LX074)
n = 85
(e)
Metagreywacke
(LX076)
n = 92
(f)
Metasandstone
(CT005)
n = 70
(g)
Mylonitized metagranodiorite
(LX062)
n = 50
(h)
Gneissic metagranodiorite
(LX056)
n = 51
(i)
MORB
MORB–DM
Island arc
CHUR
P
C
D
S
O
Cm
$\varepsilon_{Hf}(t)$
T^{C}_{DM}(Ga)
(Ga)

Figure 9.

Table 3
Summary of Hf-in-Zircon Isotopic Data for Granitoids and Metasedimentary Rocks From the Mongolian Altai Zone

Samples	Rock-type	Ages (Ma)	$\varepsilon_{Hf}(t)$	T_{DM}^{C} (Ga)
Magmatic rocks				
LX089	Metagranite	300–431	−9.5 to +8.5	1.9–0.8
LX077	Ganite vein	359–1,540	−4.2 to +13.5	2.3–0.5
LX062	Metagranodiorite	272–1,307	−13.8 to +12.6	2.2–1.0
LX056	Metagranodiorite	257–542	−22.0 to +5.1	2.7–0.9
Metasedimentary rocks				
CT006	Quartzitic sandstone	337–2,980	−25.2 to +16.0	3.6–0.4
LX086	Metagreywacke	438–1,854	−12.1 to +9.9	2.5–1.0
LX076	Metagreywacke	433–2,680	−10.0 to +12.0	3.4–0.6
LX074	Metagreywacke	166–2,521	−32.0 to +10.27	3.5–0.7
CT005	Metasandstone	461–1,250	−35.5 to +8.0	3.9–0.9

Note. The values of $\varepsilon_{Hf}(t)$ are maximum and minimum from the original data (Tables A8 and A9 in Supporting Information S1).

(LX086) consisting of medium-grained quartz, plagioclase, oriented biotite, and muscovite (micrograph in Figure 8c). Zircons from these samples are mostly bright to pale yellow to colorless, and occur as subrounded grains to euhedral and sub-euhedral prisms with a variable aspect ratio between 1:1 and 1:3. Most zircons reveal a complex texture in the cathodoluminescence (CL) images with variable luminescence and patterns, varying from low-to high luminescent homogenous to oscillatory and sector-zoning cores surrounded by variable less luminescent oscillatory rims (CL zircon inset in Figures 8a–8c). These features combined with their high Th/U ratio (>0.1, Table A3 in Supporting Information S1) suggest that the zircons represent detrital grains originating from igneous sources. Scarce and thin irregular high luminescent metamorphic rims were observed only in the sample LX086 (CL zircon inset in Figure 8c), whereas the magmatic rims with a higher Th/U ratio (>0.1) were determined in sample CT002A (CL zircon inset in Figure 8b).

From the total of 136 analyses performed in the quartz arenite CT006, 106 analyses yield concordant ages (Figure 8a) ranging from *ca.* 337 to 2,980 Ma (Table A3 in Supporting Information S1). Most of the analyses ($n = 70$) yield Cambrian-Ordovician ages from *ca.* 463 to 541 Ma with the main peak at *ca.* 494 Ma. Maximum depositional age is estimated at 475 Ma based on the 21 Ordovician zircon analyses (Figure 8a). Small distinct groups of Precambrian zircons ranging from *ca.* 771 to 2,980 Ma are also reported. Younger ages (*ca.* 438 and 338 Ma) probably resulted from a Pb loss due to metamorphic disturbance and are geologically meaningless. The Hf isotopic compositions of the Cambrian–Ordovician zircon grains cluster within the interval of −17.5 to +16.0 with T_{DM}^{C} model ages between 2.5 and 0.4 Ga, whereas the Precambrian zircon population has $\varepsilon_{Hf}(t)$ values varying from −25.2 to +8.5 with large variations in T_{DM}^{C} model ages within the Mesoproterozoic-Archean interval (Figure 9a).

From the 116 analyses performed in the litharenite CT002A, 46 analyses yield concordant ages ranging from *ca.* 347 to 652 Ma (Figure 8b and Table A3 in Supporting Information S1). Most of the concordant analyses ($n = 34$) yield Cambrian-Ordovician ages from *ca.* 461 to 491 Ma with the main peak at *ca.* 472 Ma (Figure 8b). Two secondary clusters are observed at Neoproterozoic (*ca.* 653 and 552 Ma). The youngest population is represented by six Silurian zircons, indicating a maximum depositional age at 438 Ma (Figure 8b). One Carboniferous zircon age (*ca.* 347 Ma) with a typically igneous feature and high Th/U ratio (>0.1) was registered (Figure 8b and Table A3 in Supporting Information S1).

From the 159 analyses performed in the metagraywacke LX086, 119 yield concordant ages ranging from *ca.* 393 to 1,854 Ma (Figure 8c and Table A3 in Supporting Information S1). Seventy analyses yield Cambrian-Silurian ages from *ca.* 438 to 541 Ma, with the main peak at *ca.* 518 Ma and a maximum depositional age of 446 Ma, calculated from the youngest three zircons of this group (Figure 8c). The remaining analyses produce secondary clusters with ages from *ca.* 543 to 1854 Ma and a small young cluster of Devonian ages ranging from *ca.* 393 to 416 Ma (Figure 8c). The youngest Devonian zircon analyses were obtained in a homogenous and luminescent rim that presents a low Th/U ratio (<0.1). Therefore, these ages may result from Pb loss due to a metamorphic event. The Cambrian-Ordovician zircon population of this sample records $\varepsilon_{Hf}(t)$ values between −12.1 and +6.1 with T_{DM}^{C}model ages between 2.2 Ma and 1.0 Ga, whereas older zircon grains yield both negative and positive $\varepsilon_{Hf}(t)$ values from −11.8 to +9.9 (Figure 9b).

Figure 9. $\varepsilon_{Hf}(t)$ vs. age diagrams showing results for zircons from metasedimentary and magmatic rocks collected along the NNW-SSE profile of the Mongolian Altai Zone: metasedimentary rocks from the (a–b) Northern domain (ND), (c–d) Central domain (CD), and (e) Southern domain (SD); and magmatic rocks from the (f) Lake Zone, (g) ND, and (h–i) SD. The "depleted mantle" line is after Griffin et al. (2000) and the composition of CHUR (chondritic uniform reservoir) is from Bouvier et al. (2008). The evolution line for the average mantle source to modern island-arc magmas, as well as the interval $\varepsilon_{Hf's}$ of modern mid-ocean ridge basalt (MORB) and island-arc basalts, are from Kemp and Hawkesworth (2014 and references therein).

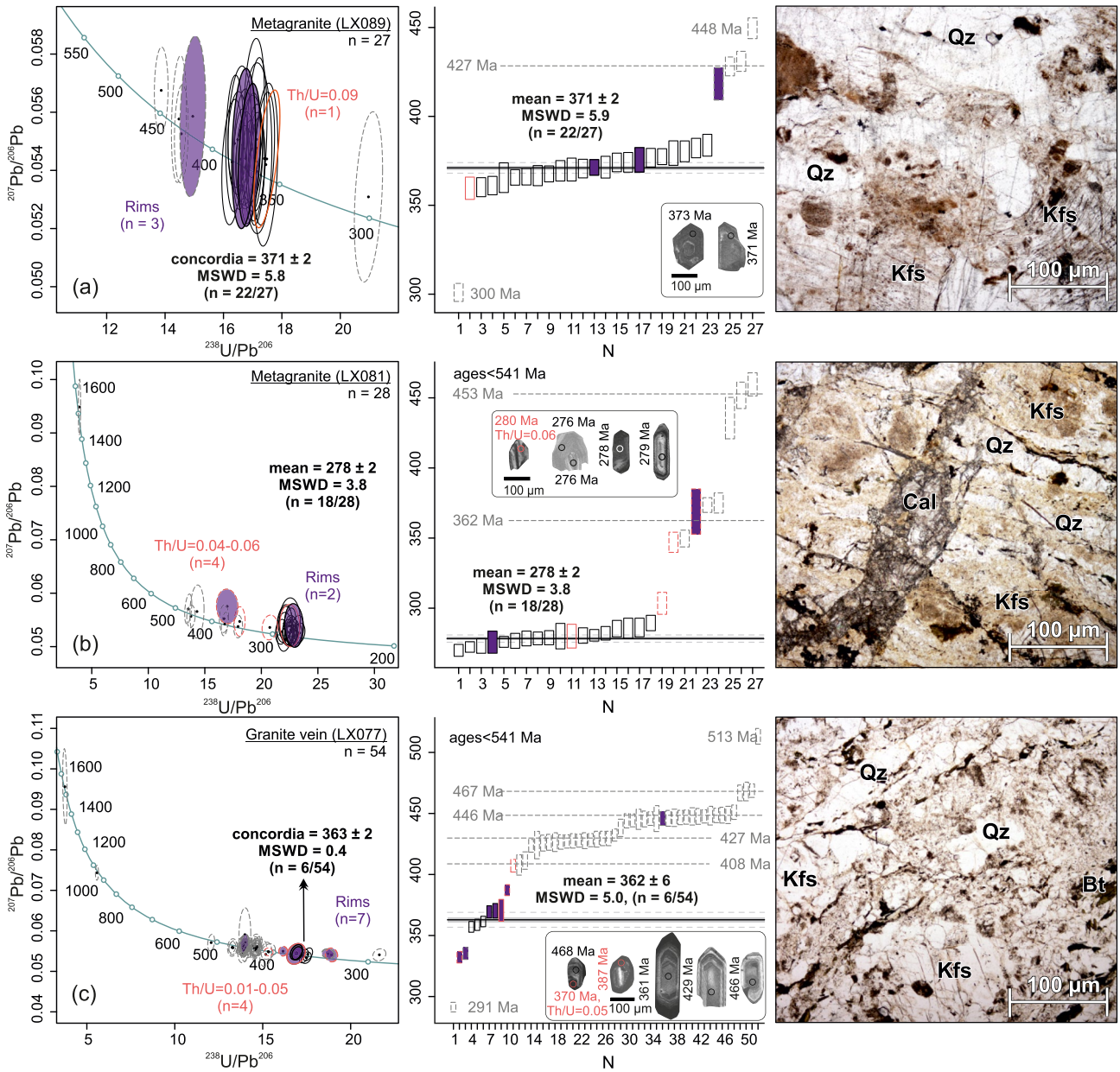

Figure 10. U-Pb Tera-Wasserburg and weighted mean diagrams for magmatic zircons of samples collected in the southernmost part of the Lake Zone and Northern domain (ND) of the studied area. The insets show representative CL images of analyzed zircons, details of the Concordia age plots, and microphotographs of the dated samples. Calculated Concordia ages are based on data from the solid ellipse lines. Dashed and gray-colored ellipses are concordant (>95%), but not included in the age calculation. Filled ellipses (purple) represent data from zircon rims, open ellipses from zircon cores. All light coral-colored ellipse lines indicate a Th/U ratio <0.1. In the Lake Zone: (a) metagranite (LX089) with coarse-grained quartz and altered feldspar. In the ND: (b) metagranite (LX081) with coarse-grained quartz, feldspar, and calcite; and (c) leucogranite vein (LX077) with coarse-grained quartz and feldspar in a fine-grained matrix of quartz, feldspar, and biotite. Locations of LA-ICP-MS analyses are shown and the numbers correspond to $^{206}Pb/^{238}U$ ages. Error ellipses and error bars are 2σ.

5.2. Magmatic Rocks From the Northern Domain

A weakly deformed metagranite (LX089) was taken from the Lake Zone, whereas a strongly deformed metagranite (LX081) and a granite vein (LX077) were collected from the ND (Figure 1 and Table 2). The metagranite sample LX089 consists of coarse-grained K-feldspar, quartz, and minor relicts of amphibole partially replaced by chlorite (micrograph in Figure 10a). The gneissified metagranite sample LX081 is mainly composed of medium-grained and elongated K-feldspar, quartz, and plagioclase, and minor biotite, muscovite, and magnetite. Calcite occurs along fractures (micrograph in Figure 10b). The granite vein sample LX077 is mainly composed of

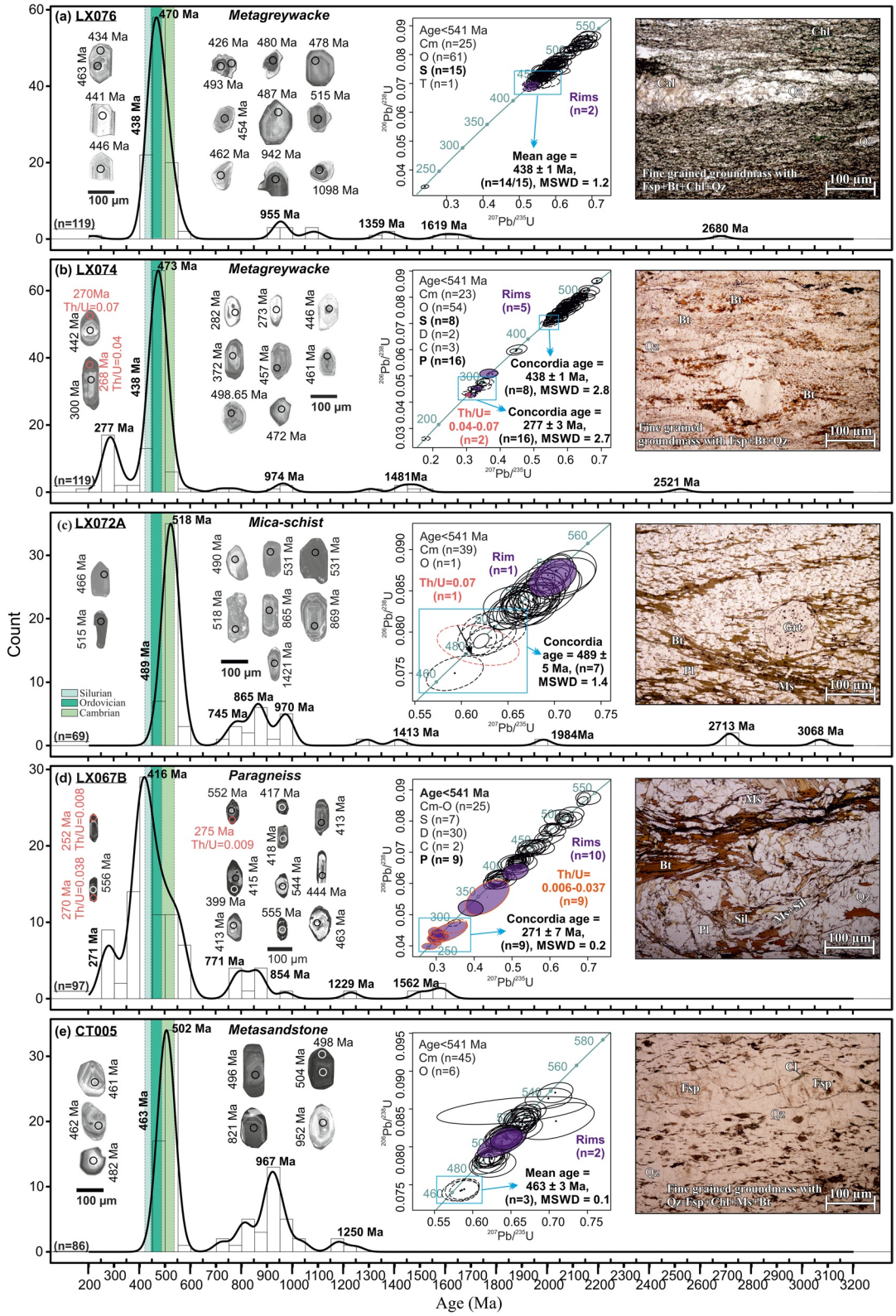
(a) LX076
Metagreywacke
(b) LX074
Metagreywacke
(c) LX072A
Mica-schist
(d) LX067B
Paragneiss
(e) CT005
Metasandstone
Count
Age (Ma)
Silurian
Ordovician
Cambrian
Age<541 Ma
Rims
Concordia age
Mean age
Fine grained groundmass with Fsp+Bt+Chl+Qz
100 μm

Figure 11.

medium-grained K-feldspar, elongated quartz and plagioclase, and fine-grained preferentially oriented biotite and minor muscovite. Epidote and relicts of amphibole partially replaced by chlorite are locally present (micrograph in Figure 10c).

Zircons from all these samples are mostly transparent, pale to bright yellow and brown to colorless. They are elongated to short prismatic with length-to-width ratios between 1:1 and 1:4, while in the zircons from the gneissic granite (sample LX089), abundant inclusions and internal fractures can also be observed. In the CL images, zircons commonly show oscillatory zoning with a variable luminescent response from the core to the rim which is typical of magmatic origins, and less commonly, insignificant luminescent homogenous and sector-zoned cores surrounded by variably thick rims (CL zircon insets in Figures 10a–10c). In the granite vein sample LX077, a few zircons have thin rims with a low luminescent homogenous pattern and low Th/U ratio (<0.01; Table A4 in Supporting Information S1), suggesting the metamorphic origin.

From the total of 67 analyses performed on zircons from the gneissic granite sample LX089, 27 analyses yield concordant ages ranging from *ca.* 300 to 449 Ma (Figure 10a and Table A4 in Supporting Information S1). The best estimate for the crystallization age was obtained from 22 concordant analyses, yielding a weighted mean $^{206}Pb/^{238}U$ age of 371 ± 2.1 Ma (MSWD = 5.9; Figure 10a). The sparse older ages (*ca.* 427 to 448 Ma) are interpreted as inherited Silurian-Ordovician zircons. Fifteen zircons have a negative initial radiogenic Hf isotopic content ($\varepsilon_{Hf}(t) = -9.5$ to -0.6; $T_{DM}^{C} = 1.9$–1.3 Ga), whereas two have positive $\varepsilon_{Hf}(t)$ values of +1.7 and +8.4 and T_{DM}^{C} model ages of 1.2 and 0.8 Ga (Figure 9c).

From the total of 51 spots analyzed in 40 zircons of the metagranite sample LX081, 43 spots were in the oscillatory and homogenous zircons, and 8 spots were in low to high luminescent rims. Twenty-eight analyses yield concordant ages ranging from *ca.* 269 to 1,468 Ma (Figure 10c and Table A4 in Supporting Information S1), and a single analysis in a dark rim yields a concordant age of *ca.* 369 Ma (see Table A4 in Supporting Information S1). Most of the analyses carried out in the core and/or oscillatory zircons ($n = 18$) yield a weighted mean $^{208}Pb/^{238}U$ age at 278.6 ± 2.5 Ma (MSWD = 3.8; Figure 10c), interpreted as the crystallization age of the granite. The remaining ages >300 Ma ($n = 10$) are interpreted as the age of inherited zircons.

From the total of 68 analyses performed in the oscillatory zircons and variables rims in the granite vein sample LX077, 47 analyses yield concordant ages. Most of the concordant analyses ($n = 32$) in the oscillatory zircons yield Ordovician-Silurian ages ranging from *ca*. 423 to 469 Ma, while two analyses produce Precambrian ages (*ca*. 1,034 and 1,540 Ma) and the remaining analyses present several sparse clusters with Devonian ages ranging from *ca.* 370 to 411 Ma (Figure 10c). Concordant ages at *ca*. to 333, 370, and 387 Ma obtained in zircon rims have a low Th/U ratio (<0.1), indicating a possible metamorphic origin (see red bars in the weighted mean diagram in Figure 10c). The best estimate for the crystallization age is calculated from six analyses, yielding a concordant age of 362 ± 2.5 Ma (MSWD = 0.48; Figure 10c). The remaining older analyses are interpreted as contamination by inherited zircons, probably sourced from the parental metasedimentary rock. The younger populations may be attributed to variable radiogenic Pb loss due to metamorphic disturbance. Thirty-eight concordant and oscillatory zircons show positive radiogenic Hf isotopic characteristics ($\varepsilon_{Hf}(t) = +3.5$ to $+13.5$; $T_{DM}^{C} = 1.1$–0.5 Ga), except for two concordant oscillatory zircon grains that present negative $\varepsilon_{Hf}(t)$ values (-4.2 and -0.9) with T_{DM}^{C} model ages of 2.3 and 1.7 Ga (Figure 9d).

5.3. Metasedimentary Rocks of the Central Domain

Zircons from two metagraywackes (LX076 and LX074) and the garnet-bearing micaschist (LX072A) were analyzed (Figure 1 and Table 2). The metagraywacke (LX076) is composed of fine-grained layers of recrystallized

Figure 11. Frequency histogram diagrams with kernel density estimate (KDE) for detrital zircon of samples collected in the Central domain (CD) and Southern domain (SD) of the studied area. The insets show representative CL images of analyzed zircons, details of the Concordia ages plots, and the microphotographs of the dated samples. Calculated Concordia ages are based on data from the dashed ellipses in the blue rectangle. Data represented by solid ellipses are concordant (>95%), but not included in the age calculation. Filled ellipses (purple) represent data from zircon rims, open ellipses from zircon cores. All lightcoral-colored ellipse lines indicate a Th/U ratio <0.1. In the CD: (a) fine-grained metagraywacke (LX076) with quartz, feldspar, biotite, chlorite, and calcite; (b) fine-to medium-grained metagraywacke (LX074) composed of quartz, feldspar, and biotite; and (c) medium-grained garnet-bearing micaschist (LX072A) with quartz, plagioclase, biotite, muscovite, garnet, and ilmenite. In the SD: (d) coarse-grained micaschist (LX067b) with quartz, plagioclase, biotite, garnet, sillimanite, and muscovite overgrowing sillimanite; and (e) fine-to medium-grained metasandstone (CT005) with quartz, feldspar, chlorite, muscovite, and biotite. Locations of LA-ICP-MS analyses are shown and the numbers correspond to $^{206}Pb/^{238}U$ ages (<1,000 Ma) and $^{207}Pb/^{206}Pb$ ages (>1,000 Ma). Error bars and error ellipses are 2σ. The age distribution for Silurian, Ordovician, and Cambrian periods is underlined by colors (see legend).

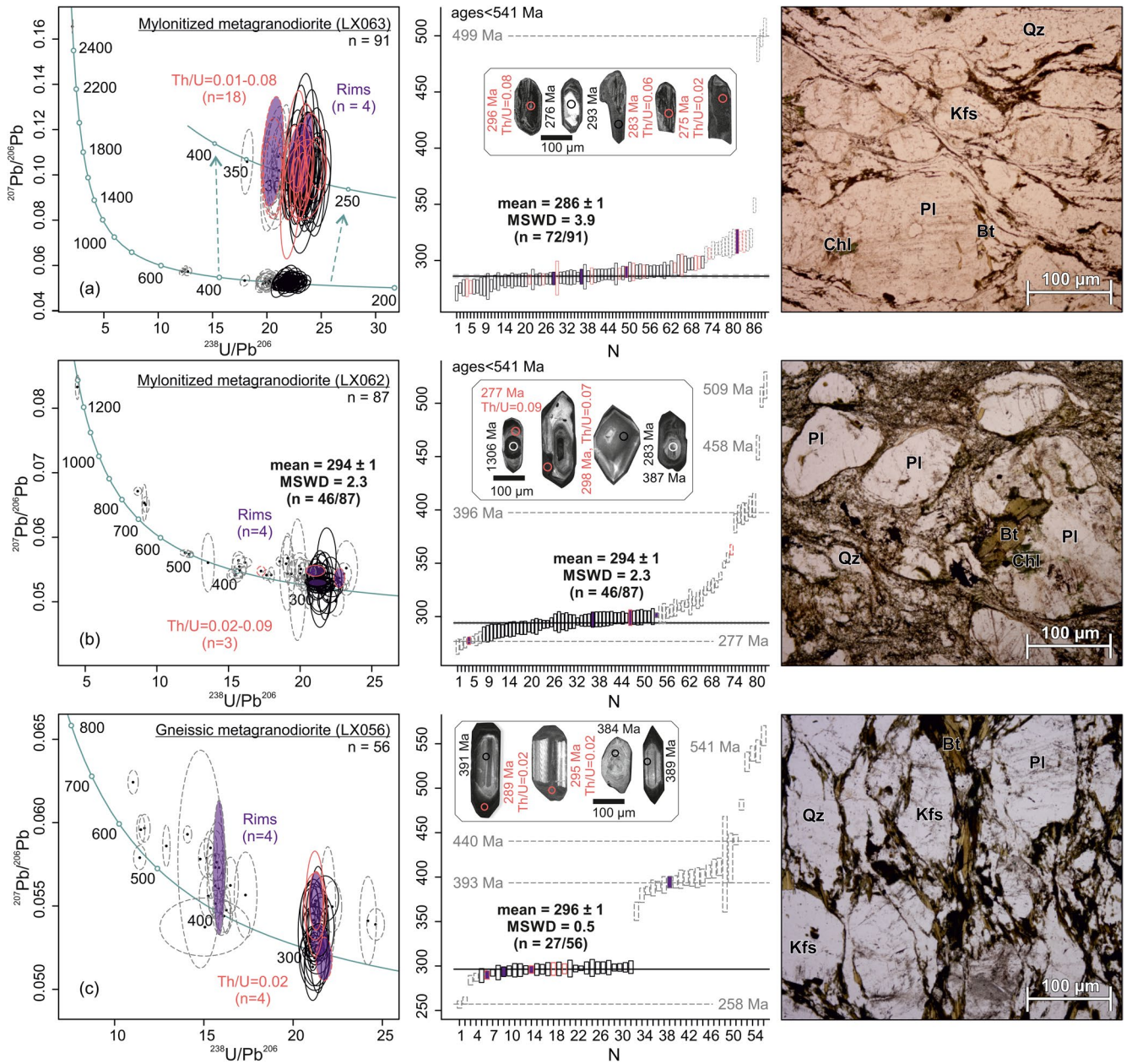

Figure 12. U-Pb Tera-Wasserburg and weighted mean diagrams for magmatic zircons of samples collected in the Southern domain (SD). The insets show representative CL images of analyzed zircons, details of the Concordia age plots, and microphotographs of the dated samples: (a) mylonitic metagranite (LX063) with coarse-grained quartz and feldspar; (b) metagranodiorite (LX062) with coarse-grained quartz and feldspar in a fine-grained matrix of quartz, feldspar, and biotite; and (c) gneissic metagranodiorite (LX056) with coarse-grained quartz, feldspar, and biotite parallel to S3 foliation. Concordia ages shown in the insets are based on data from the solid ellipse lines. Data represented by dashed and gray-colored ellipses are concordant (>95%), but not included in the age calculation. Filled ellipses (purple) represent data from zircon rims, open ellipses from zircon cores. All light coral-colored ellipse lines indicate a Th/U ratio <0.1. Locations of LA-ICP-MS analyses are shown and the numbers correspond to $^{206}Pb/^{238}U$ ages. Error ellipses and error bars are 2σ (LX063) and 1σ (LX062 and LX056), respectively.

feldspar, quartz, biotite, chlorite, and magnetite, alternating with medium-grained layers of quartz and calcite (micrograph in Figure 11a). The second metagraywacke (LX074) consists of relicts of medium to coarse-grained feldspar, quartz, and biotite surrounded by a mylonitic matrix of recrystallized feldspar, quartz, and biotite (micrograph in Figure 11b). The main metamorphic foliation of both samples is defined by the preferred orientation of elongated feldspars, biotite, and strings of opaque minerals (micrograph in Figures 11a and 11b). The micaschist (LX072A) is composed of fine-to medium-grained plagioclase, quartz, biotite, garnet, and rare muscovite. The

biotite and local muscovite are defined by metamorphic foliation folded by close-to-isoclinal folds and transposed by the axial planar cleavage (micrograph in Figure 11c).

Zircon grains from all these samples are transparent, pale to bright yellow, and brown to colorless. They are variable in size and shape, forming subrounded grains to subhedral and euhedral elongated and short prisms with a variable aspect ratio between 1:1 and 1:5. Most of the grains are broken. Under CL, they display moderately low-to high-luminescence oscillatory to homogenous and sector zoning, indicating a magmatic origin (CL zircon details inset in Figures 11a–11c). Thin irregular metamorphic rims with variable luminescence were observed only in the metagraywacke (LX074; CL zircon images in Figure 11b).

From the total of 144 analyses performed in the metagraywacke (LX076), 119 analyses yield concordant ages ranging from *ca*. 216 to 2,680 Ma (Figure 11a and Table A5 in Supporting Information S1). Most of the analyses ($n = 103$) yield Cambrian to Silurian ages ranging from *ca*. 426 to 537 Ma, with the main peak at *ca*. 470 Ma and maximum depositional age at 438 Ma, calculated from 14 Silurian zircons analyses (Figure 11a). Small groups of Precambrian ages are determined at *ca*. 955, 1,100, 1,359, 1,619, and 2,680 Ma, and only one zircon records a young age at *ca*. 216 Ma. From the 173 analyses carried out in the second metagraywacke (LX074), 119 analyses provide concordant ages ranging from *ca.* 166 to 2,521 Ma (Figure 11b and Table A5 in Supporting Information S1). Most of the analyses ($n = 87$) yield Cambrian to Silurian ages ranging from *ca*. 434 to 533 Ma, with the main peak at *ca*. 473 Ma, and three secondary clusters with Precambrian ages (*ca*. 974, 1,481, and 2,521 Ma). The maximum depositional age is calculated from the eight youngest Silurian ages, yielding a Concordia age at 438 ± 1.4 Ma (MSWD = 2.7; Figure 11b). The youngest population is represented by a Permian peak defined by 16 analyses yielding a Concordia age of 277 ± 3.5 Ma (MSDW = 2.7; Figure 11b). From this large number of Permian zircons, two analyses with a low Th/U ratio (<0.1) were obtained in dark rims and therefore may be attributed to metamorphic origin. The Hf isotopic composition of both the metagraywacke samples LX074 and LX076 are similar. Their Cambrian-Ordovician-Silurian zircon populations cluster within −6.6 to +10.2 with T_{DM}^{C}model ages from 1.8 to 0.7 Ga in the sample LX074 (Figure 9e) and between −4.4 and +12.0 with T_{DM}^{C}model ages from 1.7 to 0.6 Ga in the sample LX076 (Figure 9f). Few Precambrian zircon grains from the LX076 sample show both negative and positive $\varepsilon_{Hf}(t)$ values, clustered between −10.0 and +10.4, for which T_{DM}^{C}model ages vary from 2.5 to 0.8 Ga. The metagraywacke sample LX074 has a Precambrian zircon population with $\varepsilon_{Hf}(t)$ values bracketed between −8.6 and +1.4. The Permian populations in this sample are positive in terms of initial Hf content ($\varepsilon_{Hf}(t) = +0.6$ and +7.8), but a single Permian zircon shows a highly negative value ($\varepsilon_{Hf}(t) = -32.0$).

From the 112 analyses performed in the garnet-bearing micaschist sample LX072A, 69 analyses yield concordant ages (Figure 11c and Table A5 in Supporting Information S1). Most of the analyses ($n = 38$) yield Cambrian-Ordovician ages from *ca*. 466 to 541 Ma, with the main peak at *ca*. 518 Ma and maximum depositional age at 489 Ma, obtained from a single Ordovician zircon and six younger Cambrian zircon analyses (Figure 11c). Relatively wide groups of Precambrian ages were determined, ranging from *ca.* 745 to 3,068 Ma (Figure 11c).

5.4. Metasedimentary Rocks From the Southern Domain

Garnet-sillimanite bearing paragneiss (LX067B) and meta-sandstone (CT005; Figure 1 and Table 2) were collected from the SD. The sample LX067B consists of medium-to coarse-grained plagioclase, quartz, biotite, fibrolitic sillimanite, muscovite, and locally pinnitized cordierite. The biotite and fibrolitic sillimanite are oriented parallel to the main foliation folded by isoclinal folds (Figure 5f). This fabric is overgrown by muscovite and late retrograde chlorite (micrograph in Figure 11d). The sample CT005 is composed of a fine-grained matrix of elongated quartz and feldspar, preferentially oriented muscovite, chlorite, and minor biotite, and of coarse-grained and partially or entirely altered feldspars. Fine-grained muscovite and chlorite are oriented parallel to the main foliation (micrograph in Figure 11e).

Zircons from both samples are usually pale yellow to colorless rounded to sub-rounded grains and occasionally show subhedral to euhedral prisms, with a variable aspect ratio between 1:1 and 1:4. In the CL images, zircon grains reveal mainly igneous-related oscillatory zoning (CL zircon images in Figures 11d and 11e). However, the paragneiss sample LX067B shows zircons with oscillatory to homogeneous cores with variable CL surrounded by the thin irregular dark to gray rims with homogenous patterns and scarce dark zircons with the sector to homogenous patterns. The oscillatory zircon cores with a high Th/U ratio (>0.1; Table A6 in Supporting

Information S1) represent magmatic zircon, whereas the dark and homogenous rims and zircons have a low Th/U ratio (0.008–0.038; Table A6 in Supporting Information S1) and are interpreted as metamorphic.

From the total of 143 analyses performed in the paragneiss sample LX067B, 108 spots were analyzed in the oscillatory cores, 23 spots in the dark rims, and 12 spots in the dark zircons. From 108 analyses carried out in the oscillatory zircons and cores, just 87 analyses yield concordant ages (Figure 11d and Table A6 in Supporting Information S1). A few Precambrian clusters occur at *ca*. 771, 854, 1,229, and 1,562 Ma. Most of the cores or oscillatory zircon grains provide a wide range of ages from Devonian (*ca*. 377–420 Ma) to Cambrian-Silurian (*ca*. 437–540 Ma; Figure 11d). The three youngest zircon populations are: Silurian ($n = 8$, *ca*. 441 Ma), and two Devonian groups represented by 18 and 12 analyses, respectively, that provide weighted mean ages at *ca*. 417 and 382 Ma (Figure 11d). Fourteen analyses in the dark rims and zircons yield concordant ages from *ca.* 225 to 690 Ma. Five analyses yield a weighted mean age of *ca*. 268 Ma (MSWD = 3.21; Figure 11d). The oscillatory zircons and cores record an early Silurian maximum depositional age at *ca*. 441 Ma, whereas the Devonian zircon populations can be interpreted as a result of a Devonian high-grade metamorphic event associated with emplacement of Devonian magmatic rocks, as has been proposed in other areas of the Mongolian Altai Zone (Bibikova et al., 1992; Burenjargal et al., 2014; Hanžl et al., 2016). The Permian dark rim and zircon population is interpreted as the age of the metamorphic melting event, which is consistent with the measured low Th/U ratio (CL zircon images in Figure 11d).

From the total of 123 analyses performed in the metasandstone (CT005), 86 analyses yield concordant ages from *ca*. 461 to 1,436 Ma (Figure 11e and Table A6 in Supporting Information S1). From the 86 concordant analyses, 53 analyses yield Cambrian-Ordovician ages from *ca.* 461 to 538 Ma with the main peak at *ca.* 502 Ma, and maximum depositional age at 463 ± 3.6 Ma ($n = 3$; MSWD = 0.1; Figure 11e). Two secondary Precambrian peaks can be observed at *ca*. 967 and 1,250 Ma (Figure 11e and Table A6 in Supporting Information S1). The detrital zircons present less radiogenic Hf isotopic compositions, showing a wide range of negative $\varepsilon_{Hf}(t)$ values between −35.5 and +8.0 (Figure 9g). The $\varepsilon_{Hf}(t)$ values of the Cambrian-Ordovician zircon population with a mean peak at *ca*. 502 Ma clusters within −24.8 to +8.0, with $T_{DM}{}^{C}$model ages ranging from 3.0 to 0.9 Ga.

5.5. Magmatic Rocks From the Southern Domain

The samples LX063 and LX062 are mylonitic metagranodiorites composed of large porphyroclasts of plagioclase, K-feldspar, and quartz in a fine-grained foliated matrix defined by oriented biotite, recrystallized bends of quartz, chlorite, and by minor muscovite and epidote (micrograph in Figures 12a–12b). In contrast, the sample LX056 is a gneissic metagranodiorite composed of coarse-grained plagioclase, K-feldspar, quartz, oriented biotite, chlorite, and minor muscovite (micrograph in Figure 12c). Zircons from these all samples are mostly transparent, pale yellow to colorless, from 60 to 520 μm long and form mainly big elongated and short subhedral to euhedral prismatic grains with length/width ratios between 1:2 and 1:5. Two zircon groups can be distinguished: (a) zircons with cores with variable textures, from mostly low to rarely high luminescent oscillatory zoning to homogenous and heterogeneous patchy patterns surrounded by irregular dark luminescent and homogeneous rims; and (b) partially or entirely re-homogenized and altered individual zircons with weak zoning or no zoning (CL zircon images in Figures 12a–12c). The heterogeneous patchy cores, dark homogenous rims, and zircons have low Th/U ratios (0.02–0.09 ppm; see Table A7 in Supporting Information S1), interpreted as metamorphic overgrowth and/or recrystallization (Figures 12a–12c).

From the total of 113 analyses performed in the metagranodiorite sample LX063, 91 analyses yield concordant ages from *ca*. 163 to 2,497 Ma (Figure 12a and Table A7 in Supporting Information S1), and from the 141 analyses in the sample LX062, 87 analyses yield concordant ages ranging from *ca.* 271 to 1,276 Ma (Figure 12b and Table A7 in Supporting Information S1). The 72 concordant analyses from sample LX063 yield a mean age of 286 ± 1.3 Ma (MSWD = 3.9; Figure 12a) and 46 concordant analyses from sample LX062 provide a mean age of 294 ± 2.3 Ma (MSWD = 2.3; Figure 12b), for which the spots were mostly obtained from the homogenous patchy cores and/or dark homogenous rims. Few inherited cores record older ages, from *ca*. 305 Ma to 2,497 Ma in sample LX063 and from *ca*. 300 to 1,275 Ma in sample LX062. The best estimate for the age of the inherited cores was obtained from six analyses in sample LX062, yielding an age of *ca.* 396 Ma (Figure 12b). Therefore, we can interpret the Devonian ages as contamination by crustal rocks at the time of intrusion or as the timing of a Devonian magmatic pulse as has been defined in the area, whereas the Permian ages are interpreted as the crystallization age of the metagranodiorite samples. The remaining analyses younger than 280 or 290 Ma are

attributed to radiogenic Pb loss. Hf isotopic compositions of the metagranodiorite sample LX062 reveal two different groups explained as follows: (a) the Devonian-Carboniferous concordant zircon analyses from sample LX062 yield mainly negative $\varepsilon_{Hf}(t)$ values clustering between −13.8 and +0.98 with T_{DM}^{C} model ages from 2.2 to 1.2 Ga, and (b) the Permian zircon populations record a wide range of mixed $\varepsilon_{Hf}(t)$ values varying from −11.2 to +3.9 and T_{DM}^{C} model ages from 1.9 to 1.0 Ga (Figure 9h).

From the 82 analyses performed in the gneissic metagranodiorite sample LX056, 56 analyses yield concordant ages ranging from *ca.* 257 to 559 Ma (Figure 12c and Table A7 in Supporting Information S1). Taking into account the CL textures, most of the inherited cores yield an age of *ca.* 389 Ma, whereas the dark and homogeneous rims together with homogeneous zircons provide a Permian mean age of 296 ± 1.0 Ma (n = 27; MSWD = 0.5; Figure 12c). These data suggest that the protolith crystallized during the Permian and thus would contain few xenocrystic Devonian zircons. Hf isotopic compositions reveal two different radiogenic Hf isotopic groups explained as follows: (a) the Devonian zircon grains are characterized by large variations in negative $\varepsilon_{Hf}(t)$ values from −22 to −1.4 with T_{DM}^{C} model ages from 2.7 to 1.4 Ga, whereas (b) the Permian grains yield variable $\varepsilon_{Hf}(t)$ values from −15.5 to +5.1 and T_{DM}^{C} model ages from 2.2 to 0.9 Ga (Figure 9i).

6. Discussion

In this section, the lithological and structural data of the three studied domains are discussed together with the geochemical, geochronological, and isotopic fingerprints of metasedimentary and magmatic rocks. The findings are used to reconstruct the Cambrian to Silurian sedimentary evolution of the system and its Devonian reworking and Permian polyphase restructuration.

6.1. Tectonic Evolution

Four tectono-metamorphic events have been detected across the studied domain (Figure 3). The first deformation fabric S1 was reported only in the ND and CD in isoclinal form, often rootless folds or relics of inclusion trails captured in Barrovian minerals (Figures 2d and 5b). The main S2 fabric is associated with increasing metamorphic grade from greenschist facies in the north to higher amphibolite facies in the south. This metamorphism reaches conditions of partial melting in the southern part of the ND, while in the southern extremity of the CD it reaches the garnet zone. Structural analysis also indicates that the Devonian sheeted plutons (*ca.* 370 Ma; Cai et al., 2015) and granite vein (LX077) intruded syntectonically with the S2 fabric (Figures 1 and 2e). This corroborates with conditions of deformation of these granitoids coherent with the degree of metamorphism of the host rock; that is, metamorphic gneissosity in the north and anatectic fabrics in the south (Figure 2f). Structural data indicate that the S2 fabric was originally subhorizontal before the Permian events (Figures 3 and 4). Altogether, syntectonic intrusions of Devonian granitoids in the S2 horizontal fabric showing extensional lock up shear bands (Figure 2f) can be interpreted in terms of extension resulting in the formation of the medium to low-grade superstructure and migmatite-magmatite infrastructure (Figure 13a).

The SD reveals a third deformation fabric represented by migmatitic layering in both stromatitic to nebulitic migmatites and magmatic fabric in anatectic granitoids (Figure 3). Here, leucocratic migmatites preserve folded migmatitic S2–S3 fabrics observed in the southern part of the SD (Figures 2h–2j). This indicates, together with geochronological and isotopic arguments presented above, that the SD went through Devonian syn-D2 migmatization followed by almost complete Permian D3 re-melting. Even if the S2 and S3 foliations are presently geometrically concordant, there is a remarkably sharp metamorphic gradient between medium-grade S2 fabrics of the CD and migmatitic S3 fabrics of the SD. This indicates the presence of a major detachment separating the Permian migmatite domain in the south from the Devonian medium-to a low-grade domain in the north (Figures 3 and 13b). Taken together, the whole SD can be interpreted as a crustal-scale core complex, where the high temperature fabric is progressively retrogressed down to greenschist-facies conditions during the activity of the D3 detachment (Figures 3 and 13b). In this way, a new Permian infrastructure was originated, dominated by igneous and metamorphic rocks *ca.* 292 Ma old. The hangingwall Permian superstructure is formed by both Devonian infra- and super-structures (Figure 13b).

Subsequently, the entire structural edifice of all three domains was severely affected by the D4 deformation event, producing greenschist-facies vertical cleavage and upright E-W folds with sub-horizontal hinges in all domains (Figures 2c, 2g, 2k, and 3). This implies that all domains were exhumed to upper crustal conditions before D4.

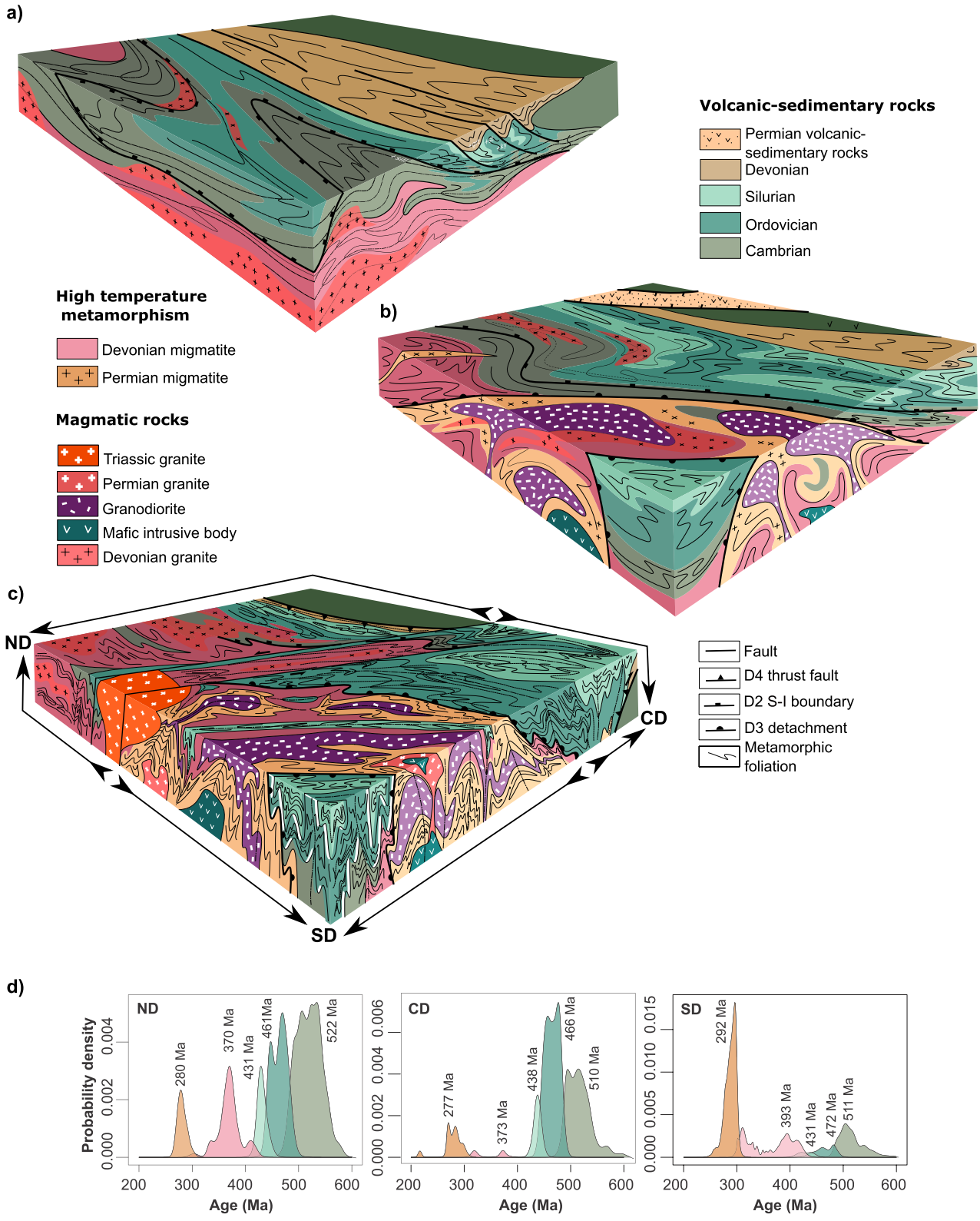
a)
Volcanic-sedimentary rocks
Permian volcanic-sedimentary rocks
Devonian
Silurian
Ordovician
Cambrian
High temperature metamorphism
Devonian migmatite
Permian migmatite
Magmatic rocks
Triassic granite
Permian granite
Granodiorite
Mafic intrusive body
Devonian granite
b)
c)
ND
CD
SD
Fault
D4 thrust fault
D2 S-I boundary
D3 detachment
Metamorphic foliation
d)
ND
280 Ma
370 Ma
431 Ma
461Ma
522 Ma
CD
277 Ma
373 Ma
438 Ma
466 Ma
510 Ma
SD
292 Ma
393 Ma
431 Ma
472 Ma
511 Ma
Probability density
Age (Ma)

Figure 13.

The D4 deformation shows important partitioning with high-strain zones localized mainly at the southern and northern boundaries of the Mongolian Altai Zone. It is responsible for the amplification of the extensional core complex in the SD and the formation of several E-W trending sub-domes and pinched upper crustal synforms. Shortening of the whole Mongolian Altai Zone led to the development of a sinistral transpressive deformation zone separating the ND from the CD (Figures 3 and 13c). The zone was intruded by Triassic intrusion (Ulaan Undur granite; Cai et al., 2015) and subsequently reactivated by left-lateral strike-slip faults. Altogether, the D4 is not only responsible for important N-S shortening of the whole Mongolian Altai Zone but also for steepening of S2 and S3 fabrics and the F2 folds that were probably originally recumbent and N-S trending (Figure 13c).

6.2. Crustal Growth by Magmatic Arc and Fore-Arc Migration

The provenance and depositional setting of sediments can be deduced from their whole-rock geochemistry (e.g., Bhatia & Crook, 1986; Roser & Korsch, 1988). Accordingly, the subarkose samples (CT001 and CT005) and quartz arenite sample (CT006) reflect a quartzose sedimentary provenance. The graywacke samples (LX076, LX074, and LX086) reflect felsic igneous and intermediate igneous provenances, and the litharenite sample (CT002A) reflects a felsic igneous provenance (Figure A10a in Supporting Information S1). In addition, almost all the studied samples show a significant positive correlation in the La/Th ratio, which is compatible with intra-oceanic and continental island arc sources (Figure A10b in Supporting Information S1).

The estimated protolith ages of the two metasedimentary groups and their spatial distribution indicate a possible existence of two formations. In the ND, the quartz arenite sample (CT006) and the metagraywacke sample (LX086) show maximum deposition ages spreading from *ca*. 446 to 550 Ma (Figures 8a and 8c), while the litharenite sample (CT002A) displays a slightly younger maximum depositional age at *ca*. 440 Ma (Figure 8b). The two metagraywacke samples (LX076 and LX074) from the CD show similar Cambrian and Ordovician dominant age populations plus a distinct Silurian age cluster at *ca.* 438 Ma (Figures 11a and 11b). The structurally deepest garnet micaschist sample (LX072A) of the CD and the subarkose sample (CT005) from the SD display late Cambrian to early Ordovician ages (Figures 11c and 11e). Altogether, the quartz-rich metasediments from the ND to SD are probably of Ordovician maximum deposition age, while the metagraywacke and litharenite from the ND to SD are of early Silurian maximum deposition age.

The late Cambrian to early Ordovician graywackes intercalated with volcanics are known from the Habahe Group in the Chinese Altai Zone and the Tugrug and Bayantsagan formations of the Gobi-Altai domain (e.g., Broussolle et al., 2019; Jiang et al., 2017; Kröner et al., 2010). In contrast, the Ordovician Zuunnuruu and Botgonygol Formations of the Hovd domain show important siliciclastic components (Soejono et al., 2018) similarly to the studied Ordovician sediments. In addition, the Silurian maximum deposition ages of the studied metagraywackes correspond best to the graywacke-dominated Silurian Tsetseg Formation (*ca*. 442–415 Ma) of the Hovd domain (Soejono et al., 2018). Determination of the depositional environment of the studied rocks is difficult due to their metamorphic overprint. However, zircon morphologies and internal structures together with the distribution of supposed maximum depositional ages allow for estimating the sedimentary tectonic setting (Cawood et al., 2012). All the studied samples are dominated by detrital zircon ages close to their possible age of sedimentation, which indicates an active margin setting in a plot by Cawood et al. (2012) (Figure 14). Both lithological characteristics and cumulative curves of Ordovician subarkoses, quartz arenites, and Silurian litharenites thus display affinity to the metamorphic Bij group of the Hovd domain (Soejono et al., 2017, 2018, 2021). The main difference between the Bij group and Hovd domain is in the amount of metavolcanic rocks that are abundant in the Hovd domain (Buriánek et al., 2022).

The different sources of the Ordovician metasandstones (CT006 and CT005) and the Silurian metagraywacke (LX074, LX076, and LX086) are also supported by their $\varepsilon_{Hf}(t)$ in zircon data (Figures 9 and 15a). The metasandstone samples show a large proportion of Paleoproterozoic, Neoarchean, and late Meso-to Neo-proterozoic zircons

Figure 13. Structural and tectonic model of three-stage evolution of the Mongolian Altai Zone crust: (a) Devonian D1 extensional deformation of the Mongolian Altai Zone sedimentary sequence, forming deep migmatite infrastructure and medium to low-grade superstructure, intruded by Devonian granitoids derived from molten in; (b) development of early Permian D3 migmatite-magmatite core complex at the southern margin of the Mongolian Altai Zone associated with intrusion of granodiorite, issued from melting of Devonian lower crustal material; (c) Permian-Triassic D4 compression of the whole edifice responsible for amplification of the Permian core complex and juxtaposition of various crustal levels forming apparent "terrane" structure of the Mongolian Altai Zone; (d) columns showing the probability distribution of zircons for the Northern domain (ND), Central domain (CD), and Southern domain (SD). These patterns show that each domain is characterized by similar depositional and Devonian magmatic-metamorphic history, but differs markedly in Permian reworking, which dominates in the SD-Tseel domain.

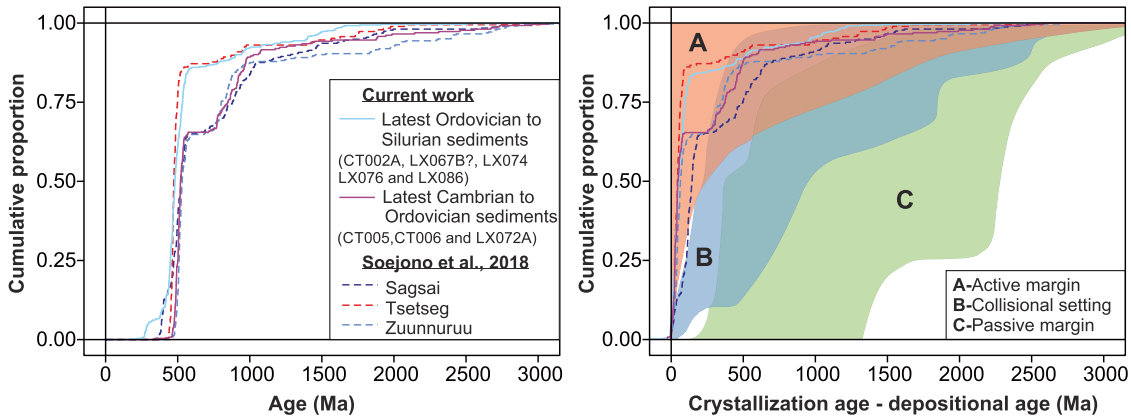

Figure 14. (a) Cumulative distribution curves of detrital zircon age spectra, and (b) cumulative distribution curves of differences between the crystallization ages (CA) and depositional ages (DA) of the detrital zircons from metasandstone and metagraywacke samples of the Northern domain (ND), Central domain (CD), and Southern domain (SD) from the current work (solid lines) and published data (dotted lines) from the Zuunnuruu, Tsetseg, and Sagsai formations of the Hovd domain (Soejono et al., 2018).

with mostly negative $\varepsilon_{Hf}(t)$ values, while Cambrian to Ordovician zircons reveal both negative and positive $\varepsilon_{Hf}(t)$ values (Figures 9a, 9g, and 15a), which is a feature typical for other parts of the Mongolian and Chinese Altai zones (Figures 15b and 15c). The Archean to Neoproterozoic zircons are possibly derived from northerly Baydrag and Zavkhan continental blocks of the CMM (Bold et al., 2016; Broussolle et al., 2019; Jiang et al., 2017), while

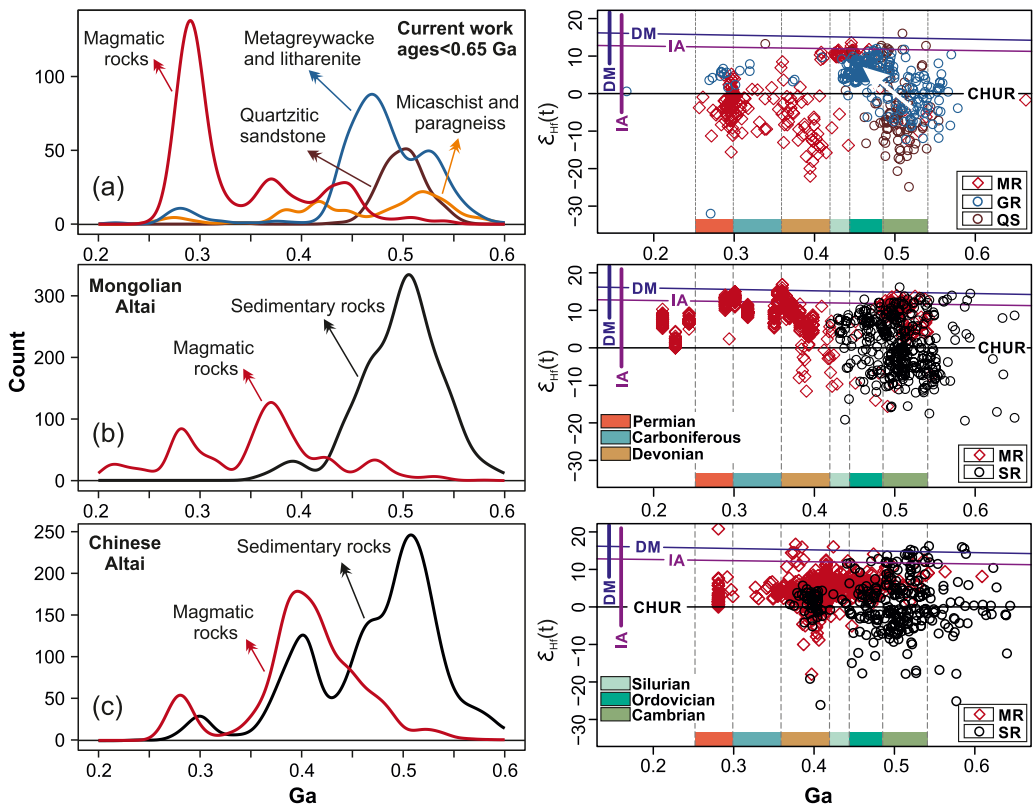

Figure 15. Comparison of KDE of all new U-Pb zircon data and binary plots of all new hafnium isotopic data (a) obtained in this study; and all previous U-Pb and Hf isotopic data from (b) the Mongolian Altai Zone (U-Pb: Burenjargal et al., 2016; Cai et al., 2015; Jiang et al., 2012, 2017; Hanžl et al., 2016; Long et al., 2020; Soejono et al., 2017, 2018 and zircon-Hf: Cai et al., 2015; Janoušek et al., 2018; Long et al., 2020; Jiang et al., 2012, 2017) (c) and the Chinese Altai Zone (U-Pb: Broussolle et al., 2018; Cai et al., 2011a; Cai et al., 2011b; Dong et al., 2018; Jiang et al., 2011; Long et al., 2007; Sun et al., 2008, 2009; Y. Wang et al., 2014 and zircon-Hf: Broussolle et al., 2020; Cai et al., 2011a; Cai et al., 2011b; Jiang et al., 2011; Long et al., 2007; Sun et al., 2008, 2009).

the Cambrian and Ordovician zircon populations correspond to the Ikh Mongol arc granitoids that intruded the late Archean to Paleoproterozic interior of Mongolian continental blocks (Figure 16a). On the other hand, the metagraywacke samples display only minor presence of Meso-to Neo-proterozoic and Cambrian-Ordovician zircons with negative and mainly positive $\varepsilon_{Hf}(t)$ values, while their Silurian zircons are characterized by dominantly positive $\varepsilon_{Hf}(t)$ values (Figures 9b, 9e, 9f, and 15a). This trend is less pronounced in published data from the Mongolian Altai Zone (Figure 15b) and absent from the Chinese Altai Zone rocks (Figure 15c). The increase of juvenile material in the source of the Silurian metagraywackes can be interpreted in terms of the derivation of sediments from the magmatic arc, which intruded the Grenville-age active margin of the Baydrag and/or Lake Zone ophiolite sequence (Figure 16b). This source is less important in other parts of the Altai range.

6.3. Devonian and Permian Magmatic Cratonization of Sedimentary Pile

There are two age groups of magmatic rocks: the Devonian granites preserved in the Lake Zone and the ND, and Permian granitoids dominating the SD (Figure 1). These two groups of rocks are well developed in other parts of the Mongolian and Chinese Altai zones as well (Figures 7, 15b, and 15c). The studied Devonian granitoids correspond to S- and I-type felsic igneous rocks typical of active continental margins (Burenjargal et al., 2016; Cai et al., 2015; Huang et al., 2020; Jiang et al., 2016) and the Permian ones show spatial and compositional continuity with *ca*. 270–280 Ma A- and S-type granitoids concentrated along the southern margin of the Chinese Altai Zone (Y. Tong et al., 2014).

The main pattern of the Hf isotopic signature in zircon from magmatic rocks of the Mongolian and Chinese Altai zones shows that a major change in the form of Lu-Hf fractionation occurred suddenly around the early Devonian (*ca*. 400 Ma; Figures 15b and 15c). This dramatic change was interpreted in terms of major input of more juvenile material responsible for positive initial epsilon hafnium values in Devonian granitoids (Cai et al., 2015; Cai et al., 2011a; Cai et al., 2011b; M. Sun et al., 2009). However, Devonian Lake Zone granite (LX089) shows markedly negative $\varepsilon_{Hf}(t)$ values (Figures 9c and 15a), implying melting of an old Precambrian, possibly Baydrag (CMM) basement located beneath the Lake Zone ophiolitic nappe (Figure 16c). On the other hand, the granite vein (LX077) from the southern part of the ND dated at *ca.* 370 Ma shows mainly positive ε_{Hf} (t) values (Figures 9d and 15a), which is consistent with the possible melting of Silurian immature sediments (Figure 16c). The studied Permian igneous rocks show a Devonian source (sample LX081 in Figure 10b, and samples LX062 and LX056 in Figures 12b and 12c), as is indicated by the *ca.* 380 Ma age peak of inherited zircons. In addition, an important Devonian peak in sillimanite paragneiss (LX067 B) suggests that the Permian high-grade gneisses of the SD underwent an important Devonian melting event (Figure 16d), which is also supported by negative ε_{Hf} (t) signatures of Permian zircons and their Proterozoic model ages. Unlike juvenile Permian magmatism dominating other parts of the Mongolian and Chinese Altai zones (Figures 15b and 15c), the source of Permian granitoids is probably the Devonian migmatitic infrastructure (Figure 16).

6.4. Summary of the Geodynamic Evolution of the Mongolian Altai Zone in Southwestern Mongolia

The Mongolian Altai Zone was traditionally interpreted as a collage of three oceanic and continental terranes represented by the Hovd, Gobi-Altai, and Tseel domains (Badarch et al., 2002; Wilhem et al., 2012; Windley et al., 2005), while Tomurtogoo (2012, 2017) subdivided its structure into five zones. Another view is that the Mongol Altai Zone is a single giant accretionary wedge developed above the long-lasting Pacific-type subduction system (Jiang et al., 2017, 2012; Long et al., 2008; Soejono et al., 2018; Xiao et al., 2004, 2009). In contrast, Broussolle et al. (2019) and Guy et al. (2020) proposed that at least the Chinese Altai Zone crustal structure resulted from the juxtaposition of contrasting orogenic crustal levels along steeply inclined boundaries.

Several units of the Mongolian Altai Zone contain serpentinite mélanges (Ulgii zone), ultramafic and gabbroic mélanges (Hovd zone), or associations of serpentinites, gabbros, and metabasalts (Tsagaanshuvuut zone), interpreted as remnants of dismembered ophiolites possibly of late Proterozoic–lower Cambrian age (Dergunov et al., 2001; Khukhuudei et al., 2020). However, the age of these rocks has not been defined isotopically, and in some places even represent underlying Lake Zone Neoproterozoic to Cambrian ophiolite rocks imbricated with the Mongolian Altai Zone sequences, as is the case of the Hovd domain (Soejono et al., 2017). It has since been argued that the Ordovician siliciclastic sediments of the Zuunuruu formation were deposited either on a hyperextended Precambrian continental margin and the Lake Zone ophiolite, or on a newly formed fore arc oceanic crust (Buriánek et al., 2022).

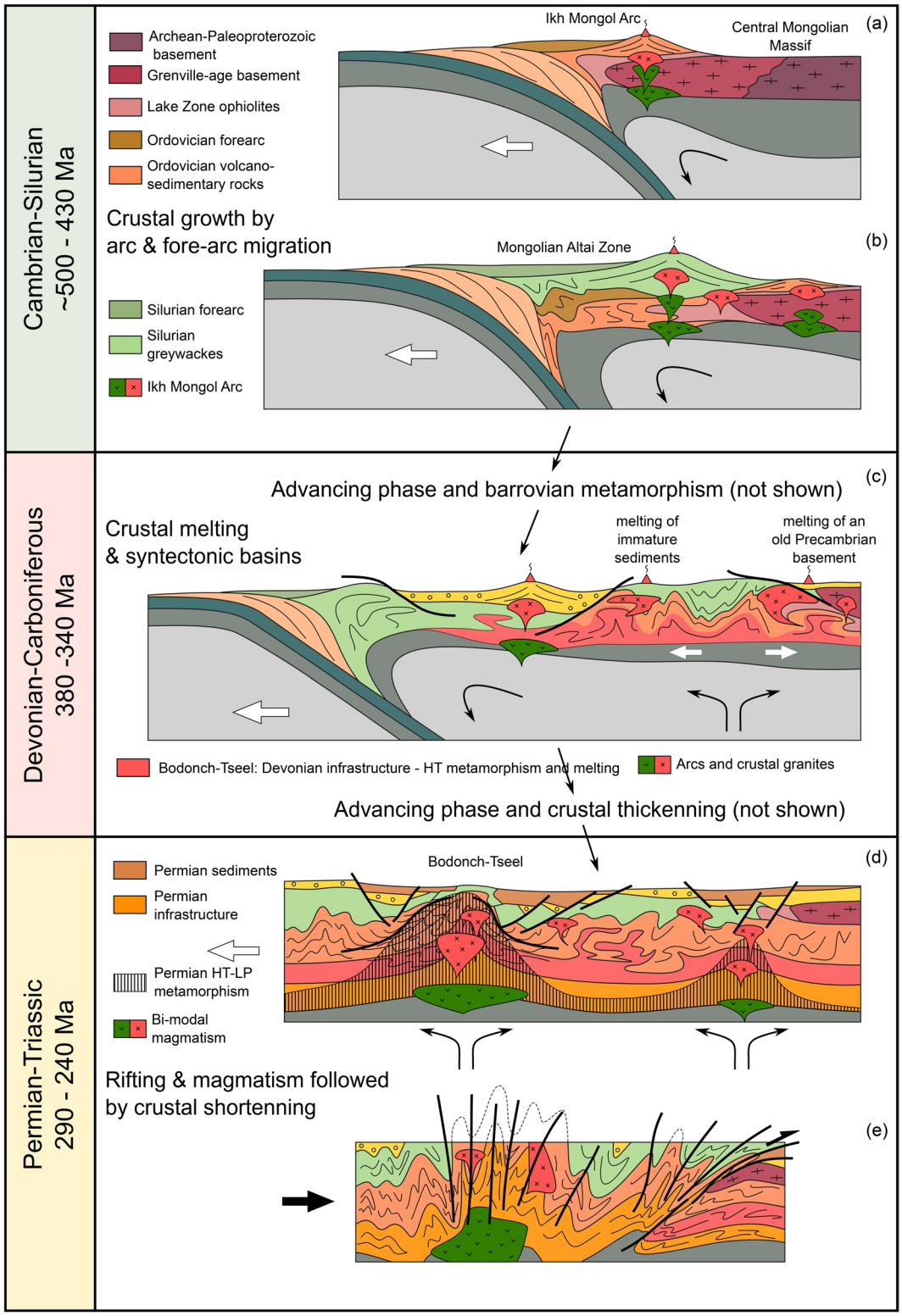

Figure 16.

This study provides evidence that the early Paleozoic sequences of the Mongolian Altai Zone in southwestern Mongolia originated by sediment transport from an adjacent voluminous magmatic arc source, which migrated from the continent toward the trench (Figure 16), as proposed by Janoušek et al. (2018). This evolution can be interpreted in terms of a Cambrian-Ordovician fore-arc basin filled with dominantly

continental arc and the CMM cratonic crust-derived components (Figure 16a), progressively evolving into a purely magmatic arc source during the late Ordovician and Silurian rollback of the oceanic plate (Figure 16b). The entire sequence was later affected by Barrovian-type metamorphism associated with crustal thickening, which in turn is considered as a result of a short-lived advancing subduction mode (Jiang et al., 2019; Soejono et al., 2021). The age of this event is not well-constrained, but has to have occurred after the deposition of Silurian graywackes and before the middle to late Devonian magmatism. The latter event is manifested by partial melting connected to crustal-scale extension (Figure 16c) related to renewed oceanic rollback (e.g., Jiang et al., 2016, 2019). This event is accompanied by the development of important Devonian terrigenous and carbonates sedimentation described in the Gobi-Altai and Hovd domains (Buriánek et al., 2022), and possibly also in the Ulgii domain.

The structural and isotopic data show that the Permian thermal event is marked by the development of a large-scale extensional core complex associated with massive re-melting of the Devonian lower crust. In the Chinese Altai Zone, the Permian high temperature event is well known and attributed to an extensional intra-plate setting (L. H. Chen & Han, 2006; C. L. Zhang et al., 2012) related to a mantle plume activity (L. X. Tong et al., 2013; Y. Tong et al., 2014). However, recent studies by Broussolle et al. (2018) attributed granulite-facies metamorphism and magmatism to a Permian collision between the East Junggar basement and the Chinese Altai Zone. This event was manifested by vertical extrusions of the partially molten lower crust, emplacement of syntectonic gabbros and granitoids (Broussolle et al., 2018), and pegmatite dyke swarms perpendicular to the Permian orogenic front (Jiang et al., 2019). The heat source for the elevated Permian thermal regime was seen in heterogeneous perturbation of the mantle in front of the advancing East Junggar indenter.

The present study can reconcile these two contrasting views. The large extensional core complex represents an extremely stretched and thermally reworked southern part of the Mongolian Altai Zone crust (Figure 16d). The described early Permian migmatites and granitoids coincide with the Bodonch-Tseel domain, and continue further west as a similar Permian magmatic and metamorphic province in the Chinese Altai Zone. The southern part of the Mongolian Altai Zone east of the studied region was interpreted as an early Permian rift, characterized by rhyolite and basaltic extrusions and associated siliciclastic sedimentation (Kovalenko et al., 2004; Yarmolyuk et al., 2013) and granitoid intrusions (Kröner et al., 2010). Similar rift zones were also described at the northern margin of the Mongolian Altai Zone and in the Trans-Altai Zone to the south and were well imaged by potential field methods (Guy et al., 2014, 2020, 2021). The whole Bodonch-Tseel domain likely represents a lower crustal expression of this giant Permian rift system that was shortened during the subsequent mid-Permian to Triassic collision as documented in the Chinese Altai Zone (Jiang et al., 2012, 2019; Figure 16e). In the Mongolian Altai Zone, this compressive event was expressed by the amplification of extensional core complexes that were converted to a series of domes and pinched basins.

Altogether, both the suspect terrane amalgamation and the accretionary wedge models of the Mongolian Altai Zone should be reconsidered. The ocean plate stratigraphy, a necessary prerequisite for the oceanic accretionary system (Kusky et al., 2013), was not proved in the studied transect. Instead, the Cambrian-Ordovician mature and early Silurian immature sedimentary sequences indicate progressive evolution of the supra-subduction marginal basin. The three studied domains share similar Devonian and earlier metamorphic and magmatic history, but differ in degree of early Permian reworking, which is most pronounced in the Bodonch-Tseel domain. The geodynamic significance of Permian extensional processes and subsequent shortening needs to be further re-evaluated in the light of the recently proposed late Paleozoic to Permian-Triassic multiple roll-back and oroclinal bending model of Xiao et al. (2018).

Figure 16. Idealized geodynamic cartoon showing the Cambrian to Triassic tectonic evolution of the Mongolian Altai Zone: (a) formation of the fore-arc basin in front of Cambrian-Ordovician continental arc (Ikh-Mongol), established above the stretched southern margin of the Baydrag Block; (b) Ordovician-Silurian retreat of subduction zone related to the migration of the arc toward the younger juvenile crust. Arc-derived graywackes are filling the proximal fore-arc basin and show a mainly juvenile signature. The late Silurian-early Devonian thickening of the fore-arc basin and accretionary wedge related to Barrovian-type metamorphism is not shown; (c) Devonian crustal thinning and anatexis of a preexisting Cambrian-Silurian meta-sedimentary package associated with emplacement of peraluminous granitoids in the middle and upper crust. The late Devonian shortening stage is not shown; (d) formation of Permian core complexes within narrow rifted and thermally reworked zones of the Mongolian Altai Zone; (e) Permian-Triassic convergence and shortening, inversion of Carboniferous-Permian basins, and development of E-W trending upright folds.

7. Conclusions

The southern sedimentary sequence of the Mongolian Altai Zone is formed by the deposition of Cambrian-Ordovician mature siliciclastic rocks followed by the deposition of early Silurian immature graywacke-type sediments. The former sequence shows Proterozoic continental and early Paleozoic arc sources while the latter rocks were derived possibly from the nearby oceanic arc. It is proposed that the entirety of the volcanic-sedimentary sequences was deposited on an extended crust in a fore-arc setting. This fore-arc basin was later affected by Barrovian metamorphism associated to post early Silurian crustal thickening event.

The deeper Cambrian-Ordovician sequence was affected by late Devonian metamorphism and melting while mid-crustal sequences were intruded by syntectonic granite sheets.

The southern part of the Mongol Altai Zone was later reworked by an early Permian magmatite and migmatite core complex which separated the hanging-wall Devonian metamorphic domains from the early Permian migmatite-magmatite core by a large-scale detachment zone. The domal structure of the early Permian core complex was later amplified during mid-Permian to Triassic shortening related to collision between the Trans-Altai Zone and Mongol Altai Zone.

The final apparent "terrane" structure is an expression of the upright folding and transpressive vertical deformation zones resulting in juxtaposition of the Devonian and Permian metamorphic domains during the mid-Permian to Triassic shortening.

Data Availability Statement

The data from both the Chinese Altai and Mongolian Altai Zones used for correlations are referenced in the figure captions of Figures 6, 7, 14 and 15. The data reported in this paper are available in the Mendeley Data Repository (https://doi.org/10.17632/x3kgmywvj6.1). The authors wish to thank Geowriters (www.geowriters.com) for proofreading and English language editing.

Acknowledgments
This work was financially supported by the EXPRO Grant 19-27682X to K. Schulmann and O. Lexa and the International Partnership Program of the Chinese Academy of Sciences (No. 132744KYSB20190039). The support of the Center for Geosphere Dynamics (UNCE/SCI/006) is acknowledged. The authors thank the Institute of Geology Mongolian Academy of Sciences for its support of the field work and for providing the maps. Arnaud Broussolle is thanked for the assistance with zircon-Hf isotopic analyses. The authors are also grateful to Prof. Vojtěch Janoušek and Vít Peřestý for their advice and assistance with zircon-Hf isotopic interpretation. Pavel Hanžl is acknowledged for providing well-organized field data sets and the organization of field expeditions in Mongolia. All original data used in this paper are available in the Supporting Information (Tables A1–A9 in Supporting Information S1).

References

Badarch, G., Dickson Cunningham, W., & Windley, B. F. (2002). A new terrane subdivision for Mongolia: Implications for the Phanerozoic crustal growth of central Asia. *Journal of Asian Earth Sciences*, *21*(1), 87–110. https://doi.org/10.1016/S1367-9120(02)00017-2

Bhatia, M. R., & Crook, K. A. W. (1986). Trace element characteristics of graywackes and tectonic setting discrimination of sedimentary basins. *Contributions to Mineralogy and Petrology*, *92*(2), 181–193. https://doi.org/10.1007/BF00375292

Bibikova, V. E., Kirnozova, T. I., Kozakov, I. K., Kotov, A. B., Neymark, L. A., Gorokhovskiy, B. M., & Shuleshko, I. K. (1992). U-Pb ages for polymetamorphic complexes on the southern flank of the Mongolian and Gobi Altai. *Geotectonics*, *26*(2), 166–172.

Blatt, H., Middleton, G. V., & Murray, R. C. (1972). *Origin of sedimentary rocks*. Prentice-Hall.

Bold, U., Crowley, J. L., Smith, E. F., Sambuu, O., & Macdonald, F. A. (2016). Neoproterozoic to early Paleozoic tectonic evolution of the Zavkhan terrane of Mongolia: Implications for continental growth in the Central Asian Orogenic Belt. *Lithosphere*, *8*(6), 729–750. https://doi.org/10.1130/L549.1

Bouvier, A., Vervoort, J. D., & Patchett, P. J. (2008). The Lu-Hf and Sm-Nd isotopic composition of CHUR: Constraints from unequilibrated chondrites and implications for the bulk composition of terrestrial planets. *Earth and Planetary Science Letters*, *273*(1–2), 48–57. https://doi.org/10.1016/j.epsl.2008.06.010

Boynton, W. V. (1984). Cosmochemistry of the rare earth elements: Meteorite studies. In P. Henderson (Ed.), *Rare earth element geochemistry* (Vol. 2, pp. 63–114). Elsevier. https://doi.org/10.1016/b978-0-444-42148-7.50008-3

Briggs, S. M., Yin, A., Manning, C. E., Chen, Z.-L., Wang, X. F., & Grove, M. (2007). Late Paleozoic tectonic history of the Ertix fault in the Chinese Altai and its implications for the development of the Central Asian Orogenic System. *Bulletin of the Geological Society of America*, *119*(7–8), 944–960. https://doi.org/10.1130/B26044.1

Broussolle, A., Aguilar, C., Sun, M., Schulmann, K., Štípská, P., Jiang, Y., et al. (2018). Polycyclic Paleozoic evolution of accretionary orogenic wedge in the southern Chinese Altai: Evidence from structural relationships and U-Pb geochronology. *Lithos*, *314–315*, 400–424. https://doi.org/10.1016/j.lithos.2018.06.005

Broussolle, A., Jiang, Y., Sun, M., Yu, Y., Wong, J., Shu, T., & Xu, K. (2020). Constraints of zircon Hf isotopes on ancient crustal reworking in the early Paleozoic Altai accretionary wedge, Central Asian Orogenic Belt. *Journal of Asian Earth Sciences*, *203*, 104538. https://doi.org/10.1016/j.jseaes.2020.104538

Broussolle, A., Štípská, P., Lehmann, J., Schulmann, K., Hacker, B. R., Holder, R., et al. (2015). P-T-t-D record of crustal-scale horizontal flow and magma-assisted doming in the SW Mongolian Altai. *Journal of Metamorphic Geology*, *33*(4), 359–383. https://doi.org/10.1111/jmg.12124

Broussolle, A., Sun, M., Schulmann, K., Guy, A., Aguilar, C., Štípská, P., et al. (2019). Are the Chinese Altai "terranes" the result of juxtaposition of different crustal levels during late Devonian and Permian orogenesis? *Gondwana Research*, *66*, 183–206. https://doi.org/10.1016/j.gr.2018.11.003

Budil, P., Hörbinger, F., & Mencl, R. (2008). Lower Devonian dalmanitid trilobites of the Prague Basin (Czech Republic). *Earth and Environmental Science Transactions of the Royal Society of Edinburgh*, *99*(2), 61–100. https://doi.org/10.1017/S1755691009006161

Burenjargal, U., Okamoto, A., Kuwatani, T., Sakata, S., Hirata, T., & Tsuchiya, N. (2014). Thermal evolution of the Tseel terrane, SW Mongolia and its relation to granitoid intrusions in the Central Asian Orogenic Belt. *Journal of Metamorphic Geology*, *32*(7), 765–790. https://doi.org/10.1111/jmg.12090

Burenjargal, U., Okamoto, A., Tsuchiya, N., Uno, M., Horie, K., & Hokada, T. (2016). Contrasting geochemical signatures of Devonian and Permian granitoids from the Tseel terrane, SW Mongolia. *Journal of Geosciences*, *61*(1), 51–66. https://doi.org/10.3190/jgeosci.210

Buriánek, D., Schulmann, K., Hrdličková, K., Hanžl, P., Janoušek, V., Gerdes, A., & Lexa, O. (2017). Geochemical and geochronological constraints on distinct Early-Neoproterozoic and Cambrian accretionary events along southern margin of the Baydrag Continent in western Mongolia. *Gondwana Research*, *47*, 200–227. https://doi.org/10.1016/j.gr.2016.09.008

Buriánek, D., Soejono, I., Schulmann, K., Janoušek, V., Hanžl, P., Čáp, P., et al. (2022). Subduction-controlled temporal and spatial variations in early Paleozoic sedimentary and volcanic record of the Mongol-Altai Domain. *Journal of Asian Earth Sciences*, *230*, 105182. https://doi.org/10.1016/j.jseaes.2022.105182

Byamba, J. (2009). Plate tectonics of the lithosphere. *Geology and mineral resource of the Mongolia series* (Vol. 4, p. 487) (in Mongolian).

Cai, K., Sun, M., Jahn, B. M., Xiao, W., Yuan, C., Long, X., et al. (2015). A synthesis of zircon U-Pb ages and Hf isotopic compositions of granitoids from Southwest Mongolia: Implications for crustal nature and tectonic evolution of the Altai Superterrane. *Lithos*, *232*, 131–142. https://doi.org/10.1016/j.lithos.2015.06.014

Cai, K., Sun, M., Yuan, C., Xiao, W., Zhao, G., Long, X., & Wu, F. (2012). Carboniferous mantle-derived felsic intrusion in the Chinese Altai, NW China: Implications for geodynamic change of the accretionary orogenic belt. *Gondwana Research*, *22*(2), 681–698. https://doi.org/10.1016/j.gr.2011.11.008

Cai, K., Sun, M., Yuan, C., Zhao, G., Xiao, W., Long, X., & Wu, F. (2011a). Prolonged magmatism, juvenile nature, and tectonic evolution of the Chinese Altai, NW China: Evidence from zircon U-Pb and Hf isotopic study of Paleozoic granitoids. *Journal of Asian Earth Sciences*, *42*(5), 949–968. https://doi.org/10.1016/j.jseaes.2010.11.020

Cai, K., Sun, M., Yuan, C., Zhao, G., Xiao, W., Long, X., & Wu, F. (2011b). Geochronology, petrogenesis, and tectonic significance of peraluminous granites from the Chinese Altai, NW China. *Lithos*, *127*(1–2), 261–281. https://doi.org/10.1016/j.lithos.2011.09.001

Cawood, P. A., Hawkesworth, C. J., & Dhuime, B. (2012). Detrital zircon record and tectonic setting. *Geology*, *40*(10), 875–878. https://doi.org/10.1130/G32945.1

Cawood, P. A., Kröner, A., Collins, W. J., Kusky, T. M., Mooney, W. D., & Windley, B. F. (2009). Accretionary orogens through Earth history. *Geological Society Special Publication*, *318*(1), 1–36. https://doi.org/10.1144/SP318.1

Chai, F., Mao, J., Dong, L., Yang, F., Liu, F., Geng, X., & Zhang, Z. (2009). Geochronology of metarhyolites from the Kangbutiebao formation in the Kelang basin, Altay Mountains, Xinjiang: Implications for the tectonic evolution and metallogeny. *Gondwana Research*, *16*(2), 189–200. https://doi.org/10.1016/j.gr.2009.03.002

Chen, B., & Jahn, B. M. (2002). Geochemical and isotopic studies of the sedimentary and granitic rocks of the Altai orogen of northwest China and their tectonic implications. *Geological Magazine*, *139*(1), 1–13. https://doi.org/10.1017/S0016756801006100

Chen, L. H., & Han, B. F. (2006). Geochronology, geochemistry and Sr-Nd-Pb isotopic composition of mafic intrusive rocks in Wuqiagou area, north Xinjiang: Constraints for mantle sources and deep processes. *Yanshi Xuebao/Acta Petrologica Sinica*, *22*(5), 1201–1214.

Collins, W. J. (2002). Nature of extensional accretionary orogens. *Tectonics*, *21*(4), 6-1–6-12. https://doi.org/10.1029/2000TC001272

Cox, K. G., Bell, J. D., & Pankhurst, R. J. (1979). Trace elements in igneous processes. *The Interpretation of Igneous Rocks*, 332–359. https://doi.org/10.1007/978-94-017-3373-1_14

Cui, X., Sun, M., Zhao, G., Zhang, Y., Yao, J., & Han, Y. (2020). Geochronological and geochemical study of the high-grade orthogneissic rocks from the Northern Fuyun Complex: Implications for crustal architecture and Early-Middle Paleozoic evolution of the Chinese Altai. *Lithos*, *366–367*, 105547. https://doi.org/10.1016/j.lithos.2020.105547

Demoux, A., Kröner, A., Hegner, E., & Badarch, G. (2009). Devonian arc-related magmatism in the Tseel terrane of SW Mongolia: Chronological and geochemical evidence. *Journal of the Geological Society*, *166*(3), 459–471. https://doi.org/10.1144/0016-76492008-090

Dergunov, A. B., Kovalenko, V. I., Ruzhentsev, S. V., & Yarmolyuk, V. V. (2001). *Tectonics, magmatism, and metallogeny of Mongolia*. Taylor and Francis Group.

Dijkstra, A. H., Brouwer, F. M., Cunningham, W. D., Buchan, C., Badarch, G., & Mason, P. R. D. (2006). Late Neoproterozoic proto-arc ocean crust in the Dariv Range, western Mongolia: A supra-subduction zone end-member ophiolite. *Journal of the Geological Society*, *163*(2), 363–373. https://doi.org/10.1144/0016-764904-156

Dong, Z., Han, Y., Zhao, G., Pan, F., Wang, K., Huang, B., & Chen, J. (2018). Zircon U-Pb ages and Hf isotopes of Paleozoic metasedimentary rocks from the Habahe Group in the Qinghe area, Chinese Altai, and their tectonic implications. *Gondwana Research*, *61*, 100–114. https://doi.org/10.1016/j.gr.2018.05.006

Filippova, I. V., Suetenko, O. D., & Levintov, M. E. (1990). Explanation text to geological map of western Mongolia in the scale 1:500,000. The volume 1, stratigraphy. (in Russian).

Gao, F. P., Zhou, G., Lei, Y. X., Wang, D. S., Chen, J. X., Zhang, H. F., et al. (2010). Early Permian granite age and geochemical characteristics in Shaerbulake of Xinjiang's Altay area and its geological significance. *Geological Bulletin of China*, *29*(9), 1281–1293.

Gao, J., & Klemd, R. (2003). Formation of HP-LT rocks and their tectonic implications in the western Tianshan Orogen, NW China: Geochemical and age constraints. *Lithos*, *66*(1–2), 1–22. https://doi.org/10.1016/S0024-4937(02)00153-6

Griffin, W. L., Pearson, N. J., Belousova, E., Jackson, S. E., Van Achterbergh, E., O'Reilly, S. Y., & Shee, S. R. (2000). The Hf isotope composition of cratonic mantle: LAM-MC-ICPMS analysis of zircon megacrysts in kimberlites. *Geochimica et Cosmochimica Acta*, *64*(1), 133–147. https://doi.org/10.1016/S0016-7037(99)00343-9

Guy, A., Schulmann, K., Munschy, M., Miehe, J. M., Edel, J. B., Lexa, O., & Fairhead, D. (2014). Geophysical constraints for terrane boundaries in southern Mongolia. *Journal of Geophysical Research: Solid Earth*, *119*(10), 7966–7991. https://doi.org/10.1002/2014JB011026

Guy, A., Schulmann, K., Soejono, I., Holzrichter, N., Lexa, O., & Munschy, M. (2021). Structures and geodynamics of the Mongolian tract of the Central Asian Orogenic Belt constrained by potential field analyses. *Gondwana Research*, *92*, 26–53. https://doi.org/10.1016/j.gr.2020.11.016

Guy, A., Schulmann, K., Soejono, I., & Xiao, W. (2020). Revision of the Chinese Altai-East Junggar terrane accretion model based on geophysical and geological constraints. *Tectonics*, *39*(4), e2019TC006026. https://doi.org/10.1029/2019TC006026

Hanžl, P., Schulmann, K., Janoušek, V., Lexa, O., Hrdličková, K., Jiang, Y., et al. (2016). Making continental crust: Origin of Devonian orthogneisses from SE Mongolian Altai. *Journal of Geosciences* (Czech Republic), *61*(1), 25–50. https://doi.org/10.3190/jgeosci.206

Helo, C., Hegner, E., Kröner, A., Badarch, G., Tomurtogoo, O., Windley, B. F., & Dulski, P. (2006). Geochemical signature of Paleozoic accretionary complexes of the Central Asian Orogenic Belt in south Mongolia: Constraints on arc environments and crustal growth. *Chemical Geology*, *227*(3–4), 236–257. https://doi.org/10.1016/j.chemgeo.2005.10.003

Hu, A., Jahn, B. M., Zhang, G., Chen, Y., & Zhang, Q. (2000). Crustal evolution and Phanerozoic crustal growth in northern Xinjiang: Nd isotopic evidence. Part I. Isotopic characterization of basement rocks. *Tectonophysics*, *328*(1–2), 15–51. https://doi.org/10.1016/S0040-1951(00)00176-1

Huang, Y., Jiang, Y., Yu, Y., Collett, S., Wang, S., Shu, T., & Xu, K. (2020). Nd-Hf isotopic decoupling of the Silurian-Devonian granitoids in the Chinese Altai: A consequence of crustal recycling of the Ordovician accretionary wedge? *Journal of Earth Science*, *31*(1), 102–114. https://doi.org/10.1007/s12583-019-1217-x

Irvine, T. N., & Baragar, W. R. A. (1971). A guide to the chemical classification of the common volcanic rocks. *Canadian Journal of Earth Sciences*, *8*(5), 523–548. https://doi.org/10.1139/e71-055

Jahn, B., Capdevila, R., Liu, D., Vernon, A., & Badarch, G. (2004). Sources of Phanerozoic granitoids in the transect Bayanhongor-Ulaan Baatar, Mongolia: Geochemical and Nd isotopic evidence, and implications for Phanerozoic crustal growth. *Journal of Asian Earth Sciences*, *23*(5), 629–653. https://doi.org/10.1016/S1367-9120(03)00125-1

Janoušek, V., Farrow, C. M., & Erban, V. (2006). Interpretation of whole-rock geochemical data in igneous geochemistry: Introducing Geochemical Data Toolkit (GCDkit). *Journal of Petrology*, *47*(6), 1255–1259. https://doi.org/10.1093/petrology/egl013

Janoušek, V., Jiang, Y., Buriánek, D., Schulmann, K., Hanžl, P., Soejono, I., et al. (2018). Cambrian-Ordovician magmatism of the Ikh-Mongol arc system exemplified by the Khantaishir magmatic complex (Lake Zone, south-central Mongolia). *Gondwana Research*, *54*, 122–149. https://doi.org/10.1016/j.gr.2017.10.003

Jiang, Y. D., Schulmann, K., Kröner, A., Sun, M., Lexa, O., Janoušek, V., et al. (2017). Neoproterozoic–early Paleozoic Peri-Pacific accretionary evolution of the Mongolian Collage System: Insights from geochemical and U-Pb zircon data from the Ordovician sedimentary wedge in the Mongolian Altai. *Tectonics*, *36*(11), 2305–2331. https://doi.org/10.1002/2017TC004533

Jiang, Y. D., Schulmann, K., Sun, M., Štípská, P., Guy, A., Janoušek, V., et al. (2016). Anatexis of accretionary wedge, Pacific-type magmatism, and formation of vertically stratified continental crust in the Altai orogenic belt. *Tectonics*, *35*(12), 3095–3118. https://doi.org/10.1002/2016TC004271

Jiang, Y. D., Schulmann, K., Sun, M., Weinberg, R. F., Štípská, P., Li, P. F., et al. (2019). Structural and geochronological constraints on Devonian suprasubduction tectonic switching and Permian collisional dynamics in the Chinese Altai, central Asia. *Tectonics*, *38*(1), 253–280. https://doi.org/10.1029/2018TC005231

Jiang, Y. D., Štípská, P., Sun, M., Schulmann, K., Zhang, J., Wu, Q. H., et al. (2015). Juxtaposition of Barrovian and migmatite domains in the Chinese Altai: A result of crustal thickening followed by doming of partially molten lower crust. *Journal of Metamorphic Geology*, *33*(1), 45–70. https://doi.org/10.1111/jmg.12110

Jiang, Y. D., Sun, M., Kröner, A., Tumurkhuu, D., Long, X., Zhao, G., et al. (2012). The high-grade Tseel terrane in SW Mongolia: An early Paleozoic arc system or a Precambrian sliver? *Lithos*, *142–143*, 95–115. https://doi.org/10.1016/j.lithos.2012.02.016

Jiang, Y. D., Sun, M., Zhao, G., Yuan, C., Xiao, W., Xia, X., et al. (2010). The ~390 Ma high-T metamorphic event in the Chinese Altai: A consequence of ridge-subduction. *American Journal of Science*, *310*(10), 1421–1452. https://doi.org/10.2475/10.2010.08

Jiang, Y. D., Sun, M., Zhao, G., Yuan, C., Xiao, W., Xia, X., et al. (2011). Precambrian detrital zircons in the early Paleozoic Chinese Altai: Their provenance and implications for the crustal growth of central Asia. *Precambrian Research*, *189*(1–2), 140–154. https://doi.org/10.1016/j.precamres.2011.05.008

Kemp, A. I. S., & Hawkesworth, C. J. (2014). *Growth and differentiation of the continental crust from isotope studies of accessory minerals. Treatise on geochemistry: Second edition* (2nd ed., Vol. 4). Elsevier Ltd. https://doi.org/10.1016/B978-0-08-095975-7.00312-0

Khain, E. V., Bibikova, E. V., Salnikova, E. B., Kröner, A., Gibsher, A. S., Didenko, A. N., et al. (2003). The Paleo-Asian ocean in the Neoproterozoic and early Paleozoic: New geochronologic data and paleotectonic reconstructions. *Precambrian Research*, *122*(1–4), 329–358. https://doi.org/10.1016/S0301-9268(02)00218-8

Khomentovsky, V. V., & Gibsher, A. S. (1996). The Neoproterozoic-lower Cambrian in northern Govi-Altay, western Mongolia: Regional setting, lithostratigraphy, and biostratigraphy. *Geological Magazine*, *133*(4), 371–390. https://doi.org/10.1017/s001675680000755x

Khukhuudei, U., Kusky, T., Otgonbayar, O., & Wang, L. (2020). The early Paleozoic mega-thrusting of the Gondwana-derived Altay-Lake Zone in western Mongolia: Implications for the development of the Central Asian Orogenic Belt and Paleo-Asian Ocean evolution. *Geological Journal*, *55*(3), 2129–2149. https://doi.org/10.1002/gj.3753

Khukhuudei, U., Kusky, T., Windley, B. F., Otgonbayar, O., & Wang, L. (2022). Ophiolites and ocean plate stratigraphy (OPS) preserved across the central Mongolian microcontinent: A new mega-archive of data for the tectonic evolution of the Paleo-Asian Ocean. *Gondwana Research*, *105*, 51–83. https://doi.org/10.1016/j.gr.2021.12.008

Kovach, V. P., Yarmolyuk, V. V., Kovalenko, V. I., Kozlovskyi, A. M., Kotov, A. B., & Terent'eva, L. B. (2011). Composition, sources, and mechanisms of formation of the continental crust of the Lake Zone of the Central Asian Caledonides. II. Geochemical and Nd isotope data. *Petrology*, *19*(4), 399–425. https://doi.org/10.1134/S0869591111030064

Kovalenko, V. I., Yarmolyuk, V. V., Kovach, V. P., Kotov, A. B., Kozakov, I. K., Salnikova, E. B., & Larin, A. M. (2004). Isotope provinces, mechanisms of generation and sources the continental crust in the Central Asian mobile belt: Geological and isotopic evidence. *Journal of Asian Earth Sciences*, *23*(5), 605–627. https://doi.org/10.1016/S1367-9120(03)00130-5

Kovalenko, V. I., Yarmolyuk, V. V., Pukhtel, I. S., Stosch, H., Jagoutz, E., & Korikovsky, S. P. (1996). Igneous rocks and magma sources of the Ozernaya zone ophiolites, Mongolia. *Petrology*, *4*(5), 420–459.

Kozakov, I. K., Didenko, A. N., Azimov, P. Y., Kirnozova, T. I., Sal'nikova, E. B., Anisimova, I. V., & Erdenejargal, C. (2011). Geodynamic settings and formation conditions of crystalline complexes in the south Altai and south Gobi metamorphic belts. *Geotectonics*, *45*(3), 174–194. https://doi.org/10.1134/S0016852111030022

Kozakov, I. K., Glebovitsky, V. A., Bibikova, E. V., Azimov, P. Y., & Kirnozova, T. I. (2002). Hercynian granulites of Mongolian and Gobian Altai: Geodynamic setting and formation conditions. *Doklady Earth Sciences*, *386*(7), 781–785.

Kozakov, I. K., Kirnozova, T. I., & Plotkina, Y. V. (2009). Age of the source of metaclastic rocks of the south Altai metamorphic belt. *Stratigraphy and Geological Correlation*, *17*, 3642.

Kozakov, I. K., Kovach, V. P., Bibikova, E. V., Kirnozova, T. I., Zagornaya, N. Y., Plotkina, Y. V., & Podkovyrov, V. N. (2007). Age and sources of granitoids in the junction zone of the Caledonides and Hercynides in southwestern Mongolia: Geodynamic implications. *Petrology*, *15*(2), 126–150. https://doi.org/10.1134/S0869591107020026

Kozakov, I. K., Kozlovsky, A. M., Yarmolyuk, V. V., Kirnozova, T. I., Fugzan, M. M., Oyunchimeg, T., & Erdenezhargal, C. (2019). Geodynamic environments of the origin of poly- and monometamorphic complexes in the southern Altai metamorphic belt, Central Asian Orogenic Belt. *Petrology*, *27*(3), 223–242. https://doi.org/10.1134/S0869591119030032

Kozakov, I. K., Sal'nikova, E. B., Yarmolyuk, V. V., Kozlovsky, A. M., Kovach, V. P., Azimov, P. Y., et al. (2012). Convergent boundaries and related igneous and metamorphic complexes in Caledonides of central Asia. *Geotectonics*, *46*(1), 16–36. https://doi.org/10.1134/S0016852112010037

Kröner, A., Lehmann, J., Schulmann, K., Demoux, A., Lexa, O., Tomurhuu, D., et al. (2010). Lithostratigraphic and geochronological constraints on the evolution of the Central Asian Orogenic Belt in SW Mongolia: Early Paleozoic rifting followed by late Paleozoic accretion. *American Journal of Science*, *310*(7), 523–574. https://doi.org/10.2475/07.2010.01

Kusky, T. M., Windley, B. F., Safonova, I., Wakita, K., Wakabayashi, J., Polat, A., & Santosh, M. (2013). Recognition of ocean plate stratigraphy in accretionary orogens through Earth history: A record of 3.8 billion years of sea floor spreading, subduction, and accretion. *Gondwana Research*, *24*(2), 501–547. https://doi.org/10.1016/j.gr.2013.01.004

Lehmann, J., Schulmann, K., Lexa, O., Corsini, M., Kröner, A., Štípská, P., et al. (2010). Structural constraints on the evolution of the Central Asian Orogenic Belt in SW Mongolia. *American Journal of Science*, *310*(7), 575–628. https://doi.org/10.2475/07.2010.02

Lehmann, J., Schulmann, K., Lexa, O., Závada, P., Štípská, P., Hasalová, P., et al. (2017). Detachment folding of partially molten crust in accretionary orogens: A new magma-enhanced vertical mass and heat transfer mechanism. *Lithosphere*, *9*(6), 889–909. https://doi.org/10.1130/L670.1

Li, Z. H., Han, B. F., & Song, B. (2004). SHRIMP zircon U-Pb dating of the Ertaibei granodiorite and its enclaves from eastern Junggar, Xinjiang, and geological implications. *Acta Petrologica Sinica*, *20*(5), 1263–1270.

Lin, Z., Yuan, C., Zhang, Y., Sun, M., Long, X., Wang, X., et al. (2019). Petrogenesis and geodynamic implications of two episodes of Permian and Triassic high-silica granitoids in the Chinese Altai, Central Asian Orogenic Belt. *Journal of Asian Earth Sciences*, *184*, 103978. https://doi.org/10.1016/j.jseaes.2019.103978

Long, X., Luo, J., Sun, M., Wang, X. C., Wang, Y., Yuan, C., & Jiang, Y. (2020). Detrital zircon U-Pb ages and whole-rock geochemistry of early Paleozoic metasedimentary rocks in the Mongolian Altai: Insights into the tectonic affinity of the whole Altai-Mongolian terrane. *Bulletin of the Geological Society of America*, *132*(3–4), 477–494. https://doi.org/10.1130/B35257.1

Long, X., Sun, M., Yuan, C., Xiao, W., & Cai, K. (2008). Early Paleozoic sedimentary record of the Chinese Altai: Implications for its tectonic evolution. *Sedimentary Geology*, *208*(3–4), 88–100. https://doi.org/10.1016/j.sedgeo.2008.05.002

Long, X., Sun, M., Yuan, C., Xiao, W., Lin, S., Wu, F., et al. (2007). Detrital zircon age and Hf isotopic studies for metasedimentary rocks from the Chinese Altai: Implications for the early Paleozoic tectonic evolution of the Central Asian Orogenic Belt. *Tectonics*, *26*(5). https://doi.org/10.1029/2007TC002128

Long, X., Yuan, C., Sun, M., Xiao, W., Wang, Y., Cai, K., & Jiang, Y. (2012). Geochemistry and Nd isotopic composition of the early Paleozoic flysch sequence in the Chinese Altai, central Asia: Evidence for a northward-derived mafic source and insight into Nd model ages in accretionary orogen. *Gondwana Research*, *22*(2), 554–566. https://doi.org/10.1016/j.gr.2011.04.009

Ludwig, K. R. (1998). On the treatment of concordant uranium-lead ages. *Geochimica et Cosmochimica Acta*, *62*(4), 665–676. https://doi.org/10.1016/S0016-7037(98)00059-3

Ludwig, K. R. (2003). *A geochronological toolkit for Microsoft Excel* (Vol. 4, p. 71). Berkeley Geochronology Center, Special Publication.

Markova, N. G., & Sharkova, T. T. (1977). Silurian and Devonian of south Mongolia (in Russian). In N. S. Zaitsev, & A. L. Yanshin (Eds.), *Osnovnye problemy geololgii Mongolii* (Vol. 22, pp. 52–61). (in Russian).

Mossakovsky, A. A., Ruzhentsev, S. V., Samygin, S. G., & Kheraskova, T. N. (1993). Central Asian fold belt: Geodynamic evolution and history of formation. *Geotectonics*, *6*, 3–33.

Nguyen, H., Hanžl, P., Janoušek, V., Schulmann, K., Ulrich, M., Jiang, Y., et al. (2018). Geochemistry and geochronology of Mississippian volcanic rocks from SW Mongolia: Implications for terrane subdivision and magmatic arc activity in the Trans-Altai Zone. *Journal of Asian Earth Sciences*, *164*, 322–343. https://doi.org/10.1016/j.jseaes.2018.06.029

Peccerillo, A., & Taylor, S. R. (1976). Geochemistry of eocene calc-alkaline volcanic rocks from the Kastamonu area, Northern Turkey. *Contributions to Mineralogy and Petrology*, *58*(1), 63–81. https://doi.org/10.1007/BF00384745

Pettijohn, F. J., Potter, P. E., & Siever, R., (1972). *Sand and sandstone*. Springer, 139(c), 66–89.

Rauzer, A. A., Zhanchiv, D. I., Golyakov, V. I., Ykhina, I. F., Ivanov, I. G., Tsukernik, A. B., & Enkhsajkhan, T. (1987). Report on results of geological survey at a scale of 1:200,000, performed in the southeast part of the Mongolian Altai, Mongolian National Republic in 1983–1986 (in Russsian).

Roberts, M. P., & Clemens, J. D. (1993). Origin of high-potassium, calc-alkaline , I-type granitoids, 7613(July 2016). https://doi.org/10.1130/0091-7613(1993)021<0825

Rojas-Agramonte, Y., Kröner, A., Demoux, A., Xia, X., Wang, W., Donskaya, T., et al. (2011). Detrital and xenocrystic zircon ages from Neoproterozoic to Paleozoic arc terranes of Mongolia: Significance for the origin of crustal fragments in the Central Asian Orogenic Belt. *Gondwana Research*, *19*(3), 751–763. https://doi.org/10.1016/j.gr.2010.10.004

Roser, B. P., & Korsch, R. J. (1988). Provenance signatures of sandstone-mudstone suites determined using discriminant function analysis of major-element data. *Chemical Geology*, *67*(1–2), 119–139. https://doi.org/10.1016/0009-2541(88)90010-1

Rudnev, S. N., Babin, G. A., Kovach, V. P., Kiseleva, V. Y., & Serov, P. A. (2013). The early stages of island-arc plagiogranitoid magmatism in Gornaya Shoriya and west Sayan. *Russian Geology and Geophysics*, *54*(1), 20–33. https://doi.org/10.1016/j.rgg.2012.12.002

Rudnev, S. N., Izokh, A. E., Borisenko, A. S., Shelepaev, R. A., Orihashi, Y., Lobanov, K. V., & Vishnevsky, A. V. (2012). Early Paleozoic magmatism in the Bumbat-Hairhan area of the Lake Zone in western Mongolia (geological, petrochemical, and geochronological data). *Russian Geology and Geophysics*, *53*(5), 425–441. https://doi.org/10.1016/j.rgg.2012.03.004

Rudnev, S. N., Izokh, A. E., Kovach, V. P., Shelepaev, R. A., & Terent'eva, L. B. (2009). Age, composition, sources, and geodynamic environments of the origin of granitoids in the northern part of the Ozernaya zone, western Mongolia: Growth mechanisms of the Paleozoic continental crust. *Petrology*, *17*(5), 439–475. https://doi.org/10.1134/S0869591109050026

Rudnev, S. N., Kovach, V. P., & Ponomarchuk, V. A. (2013). Vendian–early Cambrian island-arc plagiogranitoid magmatism in the Altai-Sayan folded area and in the Lake Zone of western Mongolia (geochronological, geochemical, and isotope data). *Russian Geology and Geophysics*, *54*(10), 1272–1287. https://doi.org/10.1016/j.rgg.2013.09.010

Ruzhentsev, S. V., & Burashnikov, V. V. (1996). Tectonics of the western Mongolian Salairides. *Geotectonics*, *5*, 379–394.

Şengör, A. M. C., Natal'in, B. A., & Burtman, V. S. (1993). Evolution of the Altaid tectonic collage and Paleozoic crustal growth in Eurasia. *Nature*, *364*(6435), 299–307. https://doi.org/10.1038/364299a0

Sengor, A. M. C., & Natalin, B. A. (1996). Paleotectonics of Asia: Fragments of a synthesis. *The tectonics of Asia. The tectonics evolution of Asia*. Cambridge University Press. Retrieved from http://www.citeulike.org/group/102/article/235706

Sláma, J., Košler, J., Condon, D. J., Crowley, J. L., Gerdes, A., Hanchar, J. M., et al. (2008). Plešovice zircon—A new natural reference material for U-Pb and Hf isotopic microanalysis. *Chemical Geology*, *249*(1–2), 1–35. https://doi.org/10.1016/j.chemgeo.2007.11.005

Soejono, I., Čáp, P., Míková, J., Janoušek, V., Buriánek, D., & Schulmann, K. (2018). Early Paleozoic sedimentary record and provenance of flysch sequences in the Hovd Zone (western Mongolia): Implications for the geodynamic evolution of the Altai accretionary wedge system? *Gondwana Research*, *64*, 163–183. https://doi.org/10.1016/j.gr.2018.07.005

Soejono, I., Buriánek, D., Janoušek, V., Svojtka, M., Čáp, P., Erban, V., & Ganpurev, N. (2017). A reworked Lake Zone margin: Chronological and geochemical constraints from the Ordovician arc-related basement of the Hovd Zone (western Mongolia). *Lithos*, *294–295*, 112–132. https://doi.org/10.1016/j.lithos.2017.08.014

Soejono, I., Peřestý, V., Schulmann, K., Čopjaková, R., Svojtka, M., Štípská, P., et al. (2021). Structural, metamorphic, and geochronological constraints on Paleozoic multi-stage geodynamic evolution of the Altai accretionary wedge system (Hovd Zone, western Mongolia). *Lithos*, *396*, 397. https://doi.org/10.1016/j.lithos.2021.106204

Štípská, P., Schulmann, K., Lehmann, J., Corsini, M., Lexa, O., & Tomurhuu, D. (2010). Early Cambrian eclogites in SW Mongolia: Evidence that the Paleo-Asian Ocean suture extends further east than expected. *Journal of Metamorphic Geology*, *28*(9), 915–933. https://doi.org/10.1111/j.1525-1314.2010.00899.x

Sukhorukov, V. P., Polyansky, O. P., Krylov, A. A., & Zinoviev, S. V. (2016). Reconstruction of the metamorphic P-T path from the garnet zoning in aluminous schists from the Tsogt Block, Mongolian Altai. *Petrology*, *24*(4), 409–432. https://doi.org/10.1134/S0869591116040068

Sun, M., Long, X. P., Cai, K., Jiang, Y., Wang, B. Y., Yuan, C., et al. (2009). Early Paleozoic ridge subduction in the Chinese Altai: Insight from the abrupt change in zircon Hf isotopic compositions. *Science in China Series D: Earth Sciences*, *52*(9), 1345–1358. https://doi.org/10.1007/s11430-009-0110-3

Sun, M., Yuan, C., Xiao, W., Long, X., Xia, X., Zhao, G., et al. (2008). Zircon U-Pb and Hf isotopic study of gneissic rocks from the Chinese Altai: Progressive accretionary history in the early to middle Paleozoic. *Chemical Geology*, *247*(3–4), 352–383. https://doi.org/10.1016/j.chemgeo.2007.10.026

Sun, S. S., & McDonough, W. F. (1989). *Chemical and isotopic systematics of oceanic basalts: Implications for mantle composition and processes* (Vol. 42, pp. 313–345). Geological Society Special Publication. https://doi.org/10.1144/GSL.SP.1989.042.01.19

Taylor, S. R., & McClennan, S. M. (1985). The continental crust: Its composition and evolution. *Geological Journal*, *21*(1), 85–88.

Togtokh, D., Baatarkhuyag, A., Gansukh, D., Bayrdlai, S., Usna-Ekh, T., Enkhbayr, B., et al. (1993). In the western Mongolia (Report No. 4861, L-46-XXIII, scale 1:200000). Government Printer (in Mongolian).

Tomurtogoo, O. (1980). Geology of Ophiolitic Complex of Mongolia. Geological Funds of Mongolia: Ulanbaatar (in Mongolian).

Tomurtogoo, O. (2012). Tectonic subdivision of orogenic belt of Mongolia. *Transactions of Institute of Geology and Mineral Resources of MAS*, *21*, 5–25. (in Mongolian).

Tomurtogoo, O. (2014). Tectonics of Mongolia. Tectonics of northern, central, and eastern Asia, explanatory note to the tectonic map of northern central eastern Asia and adjacent areas at scale, 1: 2500000. (pp. 110–126).

Tomurtogoo, O. (2017). Tectonic map of Mongolia, scale 1:3,000,000 (with brief explanatory legend on the map in Mongolian). Geological Information Centre MRPAM, Ulaanbaatar.

Tong, L. X., Chen, Y. B., Xu, Y. G., Zhou, X., & Liu, Z. (2013). Zircon U-Pb ages of the ultrahigh-temperature metapelitic granulite from the Altai orogen, NW China, and geological implications. *Acta Petrologica Sinica*, *29*(10), 3435–3445.

Tong, Y., Wang, T., Hong, D. W., Dai, Y. J., Han, B. F., & Liu, X. M. (2007). Ages and origin of the early Devonian granites from the north part of Chinese Altai Mountains and its tectonic implications. *Acta Petrologica Sinica*, *23*(8), 1933–1944.

Tong, Y., Wang, T., Jahn, B. M., Sun, M., Hong, D. W., & Gao, J. F. (2014). Post-accretionary Permian granitoids in the Chinese Altai orogen: Geochronology, petrogenesis, and tectonic implications. *American Journal of Science*, *314*(1), 80–109. https://doi.org/10.2475/01.2014.03

Tong, Y., Wang, T., Kovach, V. P., Hong, D. W., & Han, B. F. (2006). Age and origin of the Takeshiken postorogenic alkali-rich intrusive rocks in southern Altai, near the Mongolian border in China and its implications for continental growth. *Acta Petrologica Sinica*, *22*(5), 1267–1278.

Vermeesch, P. (2012). On the visualization of detrital age distributions. *Chemical Geology*, *312–313*, 190–194. https://doi.org/10.1016/j.chemgeo.2012.04.021

Vermeesch, P. (2018). IsoplotR: A free and open toolbox for geochronology. *Geoscience Frontiers*, *9*(5), 1479–1493. https://doi.org/10.1016/j.gsf.2018.04.001

Wang, S., Jiang, Y., Weinberg, R., Schulmann, K., Zhang, J., Li, P., et al. (2021). Flow of Devonian anatectic crust in the accretionary Altai orogenic belt, central Asia: Insights into horizontal and vertical magma transfer. *Bulletin of the Geological Society of America*, *133*(11–12), 2501–2523. https://doi.org/10.1130/B35645.1

Wang, T., Hong, D. W., Jahn, B. M., Tong, Y., Wang, Y. B., Han, B. F., & Wang, X. X. (2006). Timing, petrogenesis, and setting of Paleozoic synorogenic intrusions from the Altai Mountains, northwest China: Implications for the tectonic evolution of an accretionary orogen. *The Journal of Geology*, *114*(6), 735–751. https://doi.org/10.1086/507617

Wang, Y., Long, X., Wilde, S. A., Xu, H., Sun, M., Xiao, W., et al. (2014). Provenance of early Paleozoic metasediments in the central Chinese Altai: Implications for tectonic affinity of the Altai-Mongolia terrane in the Central Asian Orogenic Belt. *Lithos*, *210*, 57–68. https://doi.org/10.1016/j.lithos.2014.09.026

Wang, Y., Yuan, C., Long, X., Sun, M., Xiao, W., Zhao, G., et al. (2011). Geochemistry, zircon U-Pb ages and Hf isotopes of the Paleozoic volcanic rocks in the northwestern Chinese Altai: Petrogenesis and tectonic implications. *Journal of Asian Earth Sciences*, *42*(5), 969–985. https://doi.org/10.1016/j.jseaes.2010.11.005

Wei, C., Clarke, G., Tian, W., & Qiu, L. (2007). Transition of metamorphic series from the Kyanite- to andalusite-types in the Altai orogen, Xinjiang, China: Evidence from petrography and calculated KMnFMASH and KFMASH phase relations. *Lithos*, *96*(3–4), 353–374. https://doi.org/10.1016/j.lithos.2006.11.004

Whitney, D. L., & Evans, B. W. (2010). Abbreviations for names of rock-forming minerals. *American Mineralogist*, *95*(1), 185–187. https://doi.org/10.2138/am.2010.3371

Wilhem, C., Windley, B. F., & Stampfli, G. M. (2012). The Altaids of central Asia: A tectonic and evolutionary innovative review. *Earth-Science Reviews*, *113*(3–4), 303–341. https://doi.org/10.1016/j.earscirev.2012.04.001

Windley, B. F., Alexeiev, D., Xiao, W., Kröner, A., & Badarch, G. (2007). Tectonic models for accretion of the Central Asian Orogenic Belt. *Journal of the Geological Society*, *164*(1), 31–47. https://doi.org/10.1144/0016-76492006-022

Windley, B. F., Maruyama, S., & Xiao, W. (2005). Multiple subduction of hydrated oceanic lithosphere as the cause of the removal of hydroweakened subcontinental lithosphere under eastern China. *The Origin, Evolution and Present State of Subcontinental Lithosphere*(2), 31–33.

Xiao, W. J., Kusky, T., Safonova, I., Seltmann, R., & Sun, M. (2015). Tectonics of the Central Asian Orogenic Belt and its Pacific analogs. *Journal of Asian Earth Sciences*, *113*, 1–6. https://doi.org/10.1016/j.jseaes.2015.06.032

Xiao, W. J., Windley, B. F., Han, C., Liu, W., Wan, B., Zhang, J., et al. (2018). Late Paleozoic to early Triassic multiple roll-back and oroclinal bending of the Mongolia collage in central Asia. *Earth-Science Reviews*, *186*, 94–128. https://doi.org/10.1016/j.earscirev.2017.09.020

Xiao, W. J., Windley, B. F., Sun, S., Li, J., Huang, B., Han, C., et al. (2015). A tale of amalgamation of three permo-triassic collage systems in central Asia: Oroclines, sutures, and terminal accretion. *Annual Review of Earth and Planetary Sciences*, *43*, 477–507. https://doi.org/10.1146/annurev-earth-060614-105254

Xiao, W. J., Windley, B. F., Yuan, C., Sun, M., Han, C. M., Lin, S. F., et al. (2009). Paleozoic multiple subduction-accretion processes of the southern Altaids. *American Journal of Science*, *309*(3), 221–270. https://doi.org/10.2475/03.2009.02

Xiao, W. J., Zhang, L. C., Qin, K. Z., Sun, S., & Li, J. L. (2004). Paleozoic accretionary and collisional tectonics of the eastern Tianshan (China): Implications for the continental growth of central Asia. *American Journal of Science*, *304*(4), 370–395. https://doi.org/10.2475/ajs.304.4.370

Xu, K., Jiang, Y., Wang, S., Shu, T., Li, Z. Y., Collett, S., et al. (2021). Multi-phase tectonothermal evolution in the SE Chinese Altai, central Asia: Structures, U-Pb monazite ages and tectonic implications. *Lithos*, *392–393*, 106148. https://doi.org/10.1016/j.lithos.2021.106148

Yang, F., Mao, J., Liu, F., Chai, F., Guo, Z., Zhou, G., et al. (2010). Geochronology and geochemistry of the granites from the Mengku iron deposit, Altay Mountains, northwest China: Implications for its tectonic setting and metallogenesis. *Australian Journal of Earth Sciences*, *57*(6), 803–818. https://doi.org/10.1080/08120099.2010.495464

Yarmolyuk, V. V., Kovach, V. P., Kovalenko, V. I., Salnikova, E. B., Kozlovskii, A. M., Kotov, A. B., et al. (2011). Composition, sources, and mechanism of continental crust growth in the Lake zone of the Central Asian Caledonides: I. Geological and geochronological data. *Petrology*, *19*(1), 55–78. https://doi.org/10.1134/S0869591111010085

Yarmolyuk, V. V., Kovalenko, V. I., Sal'nikova, E. B., Kovach, V. P., Kozlovsky, A. M., Kotov, A. B., & Lebedev, V. I. (2008). Geochronology of igneous rocks and formation of the late Paleozoic south Mongolian active margin of the Siberian continent. *Stratigraphy and Geological Correlation*, *16*(2), 162–181. https://doi.org/10.1134/S0869593808020056

Yarmolyuk, V. V., Kuz'min, M. I., & Vorontsov, A. A. (2013). West Pacific-type convergent boundaries and their role in the formation of the Central Asian Fold Belt. *Russian Geology and Geophysics*, *54*(12), 1427–1441. https://doi.org/10.1016/j.rgg.2013.10.012

Yu, Y., Sun, M., Long, X., Li, P., Zhao, G., Kröner, A., et al. (2017). Whole-rock Nd-Hf isotopic study of I-type and peraluminous granitic rocks from the Chinese Altai: Constraints on the nature of the lower crust and tectonic setting. *Gondwana Research*, *47*, 131–141. https://doi.org/10.1016/j.gr.2016.07.003

Yuan, C., Sun, M., Xiao, W., Li, X., Chen, H., Lin, S., et al. (2007). Accretionary orogenesis of the Chinese Altai: Insights from Paleozoic granitoids. *Chemical Geology*, *242*(1–2), 22–39. https://doi.org/10.1016/j.chemgeo.2007.02.013

Zhang, C., Liu, L., Santosh, M., Luo, Q., & Zhang, X. (2017). Sediment recycling and crustal growth in the Central Asian Orogenic Belt: Evidence from Sr-Nd-Hf isotopes and trace elements in granitoids of the Chinese Altay. *Gondwana Research*, *47*, 142–160. https://doi.org/10.1016/j.gr.2016.08.009

Zhang, C. L., Li, Z. X., Li, X. H., Xu, Y. G., Zhou, G., & Ye, H. M. (2010). A Permian large igneous province in Tarim and Central Asian Orogenic Belt, NW China: Results of a ca. 275 Ma mantle plume? *Bulletin of the Geological Society of America*, *122*(11–12), 2020–2040. https://doi.org/10.1130/B30007.1

Zhang, C. L., Santosh, M., Zou, H. B., Xu, Y. G., Zhou, G., Dong, Y. G., et al. (2012). Revisiting the "Irtish tectonic belt": Implications for the Paleozoic tectonic evolution of the Altai orogen. *Journal of Asian Earth Sciences*, *52*, 117–133. https://doi.org/10.1016/j.jseaes.2012.02.016

Zhang, C. L., Zou, H. B., Yao, C. Y., & Dong, Y. G. (2014). Origin of Permian gabbroic intrusions in the southern margin of the Altai orogenic belt: A possible link to the Permian Tarim mantle plume? *Lithos*, *204*, 112–124. https://doi.org/10.1016/j.lithos.2014.05.019

Zhang, H., Niu, H., Terada, K., Yu, X., Sato, H., & Ito, J. (2003). Zircon SHRIMP U-Pb dating on plagiogranite from Kuerti ophiolite in Altay, north Xinjiang. *Chinese Science Bulletin*, *48*(20), 2231–2235. https://doi.org/10.1360/02wd0593

Zhang, J., Sun, M., Schulmann, K., Zhao, G., Wu, Q., Jiang, Y., et al. (2015). Distinct deformational history of two contrasting tectonic domains in the Chinese Altai: Their significance in understanding accretionary orogenic process. *Journal of Structural Geology*, *73*, 64–82. https://doi.org/10.1016/j.jsg.2015.02.007

Zhang, Z., Yan, S., Chen, B., Zhou, G., He, Y., Chai, F., et al. (2006). SHRIMP zircon U-Pb dating for subduction-related granitic rocks in the northern part of east Jungaar, Xinjiang. *Chinese Science Bulletin*, *51*(8), 952–962. https://doi.org/10.1007/s11434-008-0952-7

Zhou, G., Zhang, Z. C., Luo, S. B., He, B., Wang, X., Yin, L. J., et al. (2007). Confirmation of high temperature strongly peraluminous Mayin'ebo granites in the south margin of Altay, Xinjiang: Age, geochemistry and tectonic implications. *Acta Petrologica Sinica*, *23*(8), 1909–1920.

Zhou, G., Zhang, Z. C., Wang, X., Lou, S., He, B., & Zhang, X. (2007). Zircon U-Pb SHRIMP and 40Ar-39Ar dating of the granitic mylonite in the Mayinebo fault belt of north Xinjiang and its geological significance. *Acta Geologica Sinica*, *81*(3), 359–369.

Zonenshain, L., Kuzmin, M., Natapov, L., & Page, B. (1990). Geology of the USSR: A plate-tectonic synthesis (Vol. *21*). https://doi.org/10.1029/GD021

Zonenshain, L. P., & Kuzmin, M. I. (1978). The Khan-Taishir ophiolitic complex of western Mongolia, its petrology, origin and comparison with other ophiolitic complexes. *Contributions to Mineralogy and Petrology*, *67*(1), 95–109. https://doi.org/10.1007/BF00371637

Zorigtkhuu, O. E., Tsunogae, T., & Dash, B. (2011). Metamorphic P-T evolution of garnet-kyanite-staurolite schist and garnet amphibolite from Bodonch area, western Mongolian Altai: Geothermobarometry and mineral equilibrium modeling. *Journal of Asian Earth Sciences*, *42*(3), 306–315. https://doi.org/10.1016/j.jseaes.2011.04.026

References From the Supporting Information

Griffin, W. L., Belousova, E. A., Shee, S. R., Pearson, N. J., & O'Reilly, S. Y. (2004). Archean crustal evolution in the northern Yilgarn Craton: U-Pb and Hf-isotope evidence from detrital zircons. *Precambrian Research*, *131*(3–4), 231–282. https://doi.org/10.1016/j.precamres.2003.12.011

Jackson, S. E., Pearson, N. J., Griffin, W. L., & Belousova, E. A. (2004). The application of laser ablation-inductively coupled plasma-mass spectrometry to in situ U-Pb zircon geochronology. *Chemical Geology*, *211*(1–2), 47–69. https://doi.org/10.1016/j.chemgeo.2004.06.017

Kröner, A., Hoffmann, J. E., Xie, H., Münker, C., Hegner, E., Wan, Y., et al. (2014). Generation of early Archaean gray gneisses through melting of older crust in the eastern Kaapvaal craton, southern Africa. *Precambrian Research*, *255*(P3), 823–846. https://doi.org/10.1016/j.precamres.2014.07.017

Li, P., Sun, M., Rosenbaum, G., Jourdan, F., Li, S., & Cai, K. (2017). Late Paleozoic closure of the Ob-Zaisan Ocean along the Irtysh shear zone (NW China): Implications for arc amalgamation and oroclinal bending in the Central Asian Orogenic Belt. *Bulletin of the Geological Society of America*, *129*(5–6), 547–569. https://doi.org/10.1130/B31541.1

Paton, C., Woodhead, J. D., Hellstrom, J. C., Hergt, J. M., Greig, A., & Maas, R. (2010). Improved laser ablation U-Pb zircon geochronology through robust downhole fractionation correction. *Geochemistry, Geophysics, Geosystems*, *11*(3). https://doi.org/10.1029/2009GC002618

Söderlund, U., Patchett, P. J., Vervoort, J. D., & Isachsen, C. E. (2004). The ^{176}Lu decay constant determined by Lu-Hf and U-Pb isotope systematics of Precambrian mafic intrusions. *Earth and Planetary Science Letters*, *219*(3–4), 311–324. https://doi.org/10.1016/S0012-821X(04)00012-3

Wiedenbeck, M., Allé, P., Corfu, F., Griffin, W. L., Meier, M., & Oberli, F. (1995). Three natural zircon standards for U-Th-Pb, Lu-Hf, trace element and REE analyses. *Geostandards Newsletter*, *19*(1), 1–23. https://doi.org/10.1111/j.1751-908X.1995.tb00147.x